Product Development Report: Composite Vehicle Floor Panel

AENGM0091: Composites Design, Manufacture and Product Development

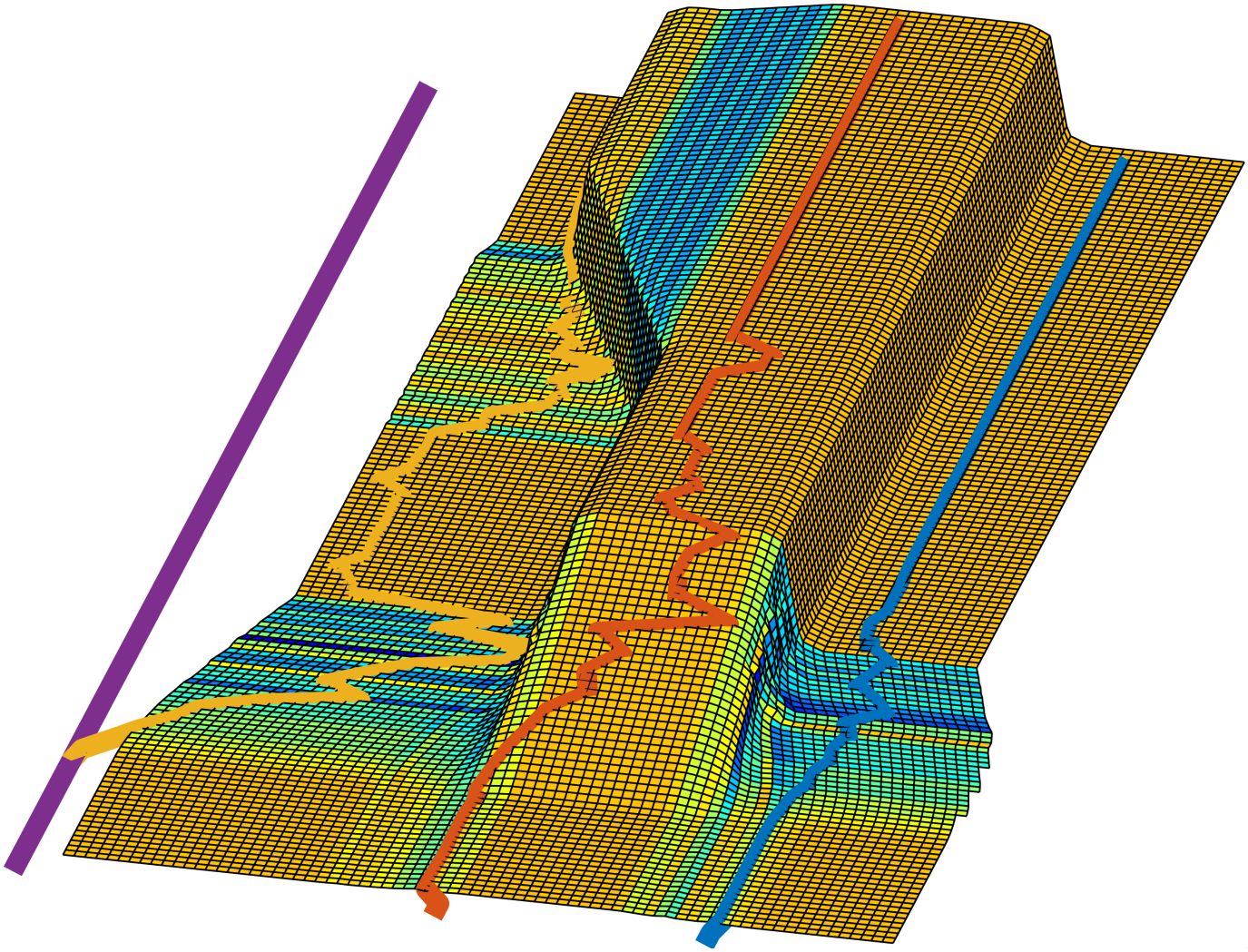

Ben Halliwell

14/12/2023

Department of Aerospace Engineering

Image: Flow front of resin over fabric during curing.

Contents

Common Symbols

Symbols

A_{coil}, A_{fibre}	Cross-sectional area	m^2
A_w	Areal density of fabric	kg/m^2
Δd	Discretisation distance	m
D	Diameter	m
E	Elastic modulus	Pa
h	Thickness of each ply	m
$K_{\parallel}, K_{\perp}$	Permeability parallel or perpendicular to the fibre direction	m^2
K_1, K_2	Permeability in the major or minor semi-axis direction	m^2
L	Length	m
$p, p_r, \Delta p_{loss}$	Applied pressure, resin pressure, frictional pressure loss	Pa
n	Number of plies	
t	Time	s
u	Velocity	m/s
V_0	Initial fibre volume fraction	
$V_{f,0}$	Minimum nominal fibre volume fraction	
V_{max}	Maximum achievable fibre volume fraction	
x, y	Position along and across part	m
β	Ratio of fibre contact length to inter-fibre spacing	
γ	Shear Angle	deg
μ	Dynamic Viscosity	Pa s
ρ_f	Density of fibres	kg/m^3
$\sigma(V_f)$	Compaction pressure	Pa

Abbreviations

CFRP	Carbon Fibre Reinforced Polymer
IDP	Initial Draping Position
NCF	Non-crimp fabric
UD	Uni-directional (preform)

Introduction

Composites, when designed and implemented correctly, can have specific strength and stiffness properties exceeding those of typical automotive materials, such as low-carbon steel and aluminium. However, the process of creating the material properties and structural form simultaneously during the manufacturing process leads to numerous technical challenges. For the automotive sector in particular, achieving manufacturing volumes in the tens of thousands of floor panels annually requires a quick cycle time to avoid requiring multiple identical tools (Verrey et al., 2006). There is also a greater emphasis for cost reduction than in the aerospace industry where weight is often the key limiting factor in design. The main driver of cost for CFRP is the price of carbon fibre itself; nonetheless, major cost savings can be made through optimising the manufacturing process by reducing energy use, complexity of manufacture and time to manufacture part (Verrey et al., 2006).

1. Geometry

Assess the key geometrical dimensions of the component (using Catia) and sketch it clearly marking the dimensions of key geometrical features.

The geometry of the vehicle floor panel is shown in Figure 1. The panel has a raised section of height 23mm, which tapers from 60 to 30mm wide with two fillets of 5.75mm each bordering the raised section. The combination of the taper and double fillet causes a double curvature, which adds complexity to the draping process. Additionally, the raised section tapers to to flat section with the radius of the lower fillet increasing from 5.75mm to a flat surface (A), which again, is difficult to drape on.

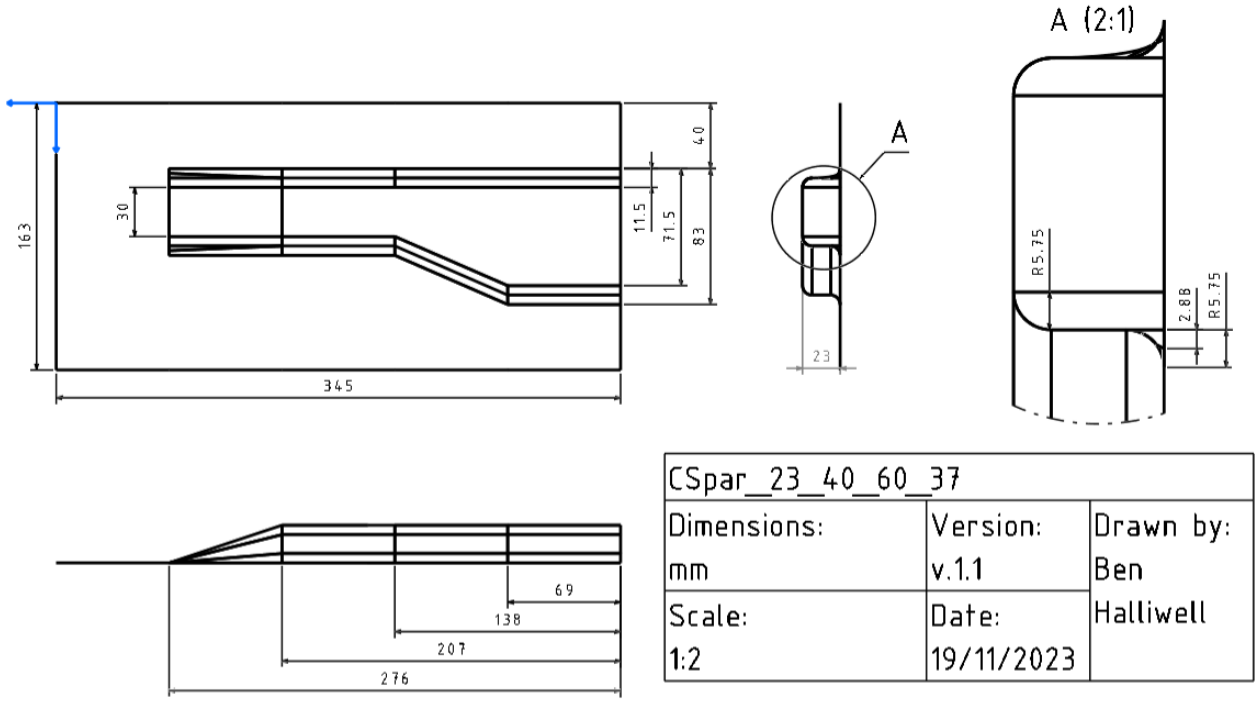

Figure 1: Technical Drawing of Composite Floor Panel

2. Draping

Consider manufacturing draping arrangement to avoid excessive deviation from the nominal fibre volume fraction (below 50% or higher than 75%). Suggest starting point for drape and any other draping arrangements. Sketch the location of shear bands. Calculate maximum shear angle within the shear bands

The draping process should be designed to minimise the variation in shearing of the fabric. Draping-induced shear has a detrimental impact on the structural performance of the part because the fibres become misaligned with the direction of loading and the fibre volume fraction is altered (Kunze et al., 2020). Additionally, shearing decreases the permeability of the fabric, which increases the characteristic flow time (Heardman et al., 2001).

2.1 Draping Optimisation

Using the KinDrape algorithm (Krogh et al., 2021), the shear angles were calculated at different draping configurations. KinDrape is a kinematic draping model, so it assumes the fabric shear stiffness is zero and the longitudinal fibre stiffness is infinite. This significantly reduces computational load compared to mechanical models, making it suited for use within optimisation algorithms. However, the assumptions lead to an overly conservative estimate of the shear angles because friction and material deformation is not considered. The KinDrape algorithm was used to calculate the mean absolute shear angle ($\bar{\gamma}_k$) of the draped fabric for different initial draping positions k, shown in figure 2. A discretisation distance (Δd) of 5mm was selected as a compromise between accuracy and computation time.

$$\bar{\gamma}_k = \frac{1}{nm} \sum_{i}^{n} \sum_{j}^{m} |\gamma_{i,j}|_k \text{ where } \gamma_{i,j} = f_{KinDrape}(x_i, y_j) \tag{1}$$

Starting the drape from around [50,65], [150,65] or [270,65] mm all give similarly low mean absolute shear angles of around 5 degrees (Figure 2).

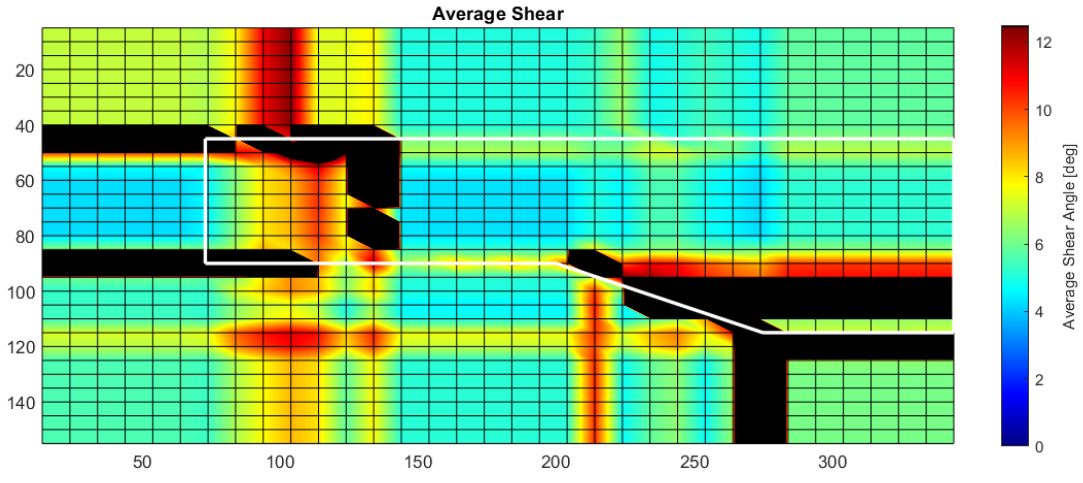

Figure 2: Average Shear Angle for Different Initial Draping Positions

The sensitivity of the mean absolute shear angle to variation in initial draping position (IDP) should also be considered because the draping process will likely be manual, and therefore the positional tolerance of the IDP will be relatively large. The draping technician will be following work instructions when draping, and diagrammatically showing a region in which to drape rather than an exact position will simplify the explanation of the process, reducing the draping time and number of errors by the assembler, which is critical for a high production volume automotive part. Starting the drape anywhere within the rectangle bounded from [0,60] to [80,80] will have a similar average shear angle to [50,65], whereas the equivalent region around [270,65] is significantly smaller (Appendix A.1). Therefore [270,65] is sub-optimal compared to the other two positions.

The black patches in figure 2 show the draping positions that KinDrape failed to produce sufficient data for. The reason for the KinDrape algorithm prematurely terminating is unclear, but it appears to correlate with the typical shear bands (Appendix A.2). KinDrape assumes a unique z coordinate for each x and y coordinate (Krogh et al., 2021), so cannot drape on vertical walls where there are multiple z coordinates for the same x and y coordinate. The floor panel does have vertical walls, so this is theorised to be the cause of premature termination. Regardless, this phenomenon is inphysical, as a small change in IDP can leads to an entirely different result (Appendix A.3), showing the limitations of the KinDrape model.

The permeability of a sheared fabric can be described with $K_1 = K_{||}\cos^2(\gamma)$ (Heardman et al., 2001). Since $u \propto K_1$ and $t \propto 1/u$ it can be reasoned that $t \propto \sec^2(\gamma)$. Therefore, the mean secanted shear angle $\hat{\gamma}_k$ is representative of the flow performance of the draping configuration (Figure 3).

$$\hat{\gamma}_k = \frac{1}{nm}\sum_{i}^{n}\sum_{j}^{m}\frac{1}{\cos^2(\gamma_{i,j})_k} \tag{2}$$

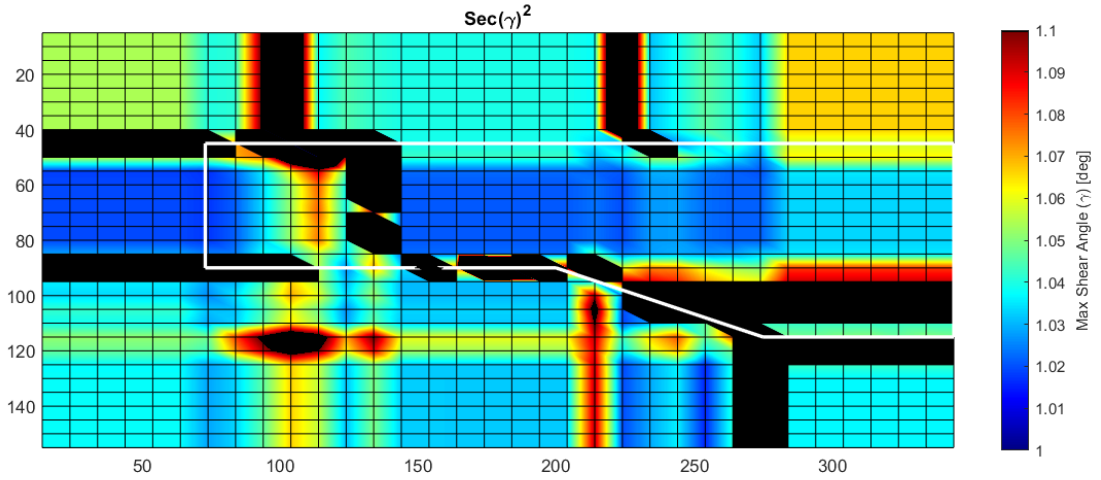

Figure 3: Average Shear Angle for Different Initial Draping Positions

However, it is still not definitive whether [50,65] or [150,65] mm is the optimum initial draping position. The $\bar{\gamma}$ simulation was repeated for $\Delta d = 2$mm (Figure 4), to increase the accuracy of the results. Decreasing the discretisation distance significantly increases computation time, so only draping positions around [50,65] and [150,65] were tested. Based on figures 2 & 3, it is assumed that since the optimal initial draping position for $\Delta d = 5$mm lies within this region, the true optimal initial draping position also lies within this region. However this is not necessarily true because with lower discretisation distance, the optimal IDP may change.

It is also assumed that with an infinitely small Δd, the optimum IDP for kinematic draping is the true IDP, which also may not be valid, as deformation or friction may cause a different draping position to be more suitable. Nonetheless, based on kinematic geodesic draping, the region around [150, 65] appears to be optimal (Figure 4).

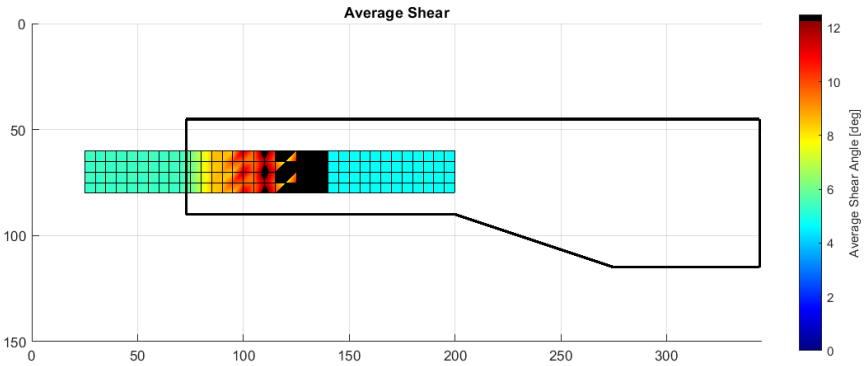

Figure 4: Average Shear Angle for Different Initial Draping Positions (Higher Resolution)

2.2 Draping from the Optimum Position

Draping from the optimal position of [150, 65] gives the shear angle distribution shown in figure 5. The mean shear angle is 4.7° with a maximum shear angle of **35.5**°. However, the majority of the fabric has almost no shear angle, with a median shear of 0.01°. A sketch of the shear bands is shown in appendix A.2.

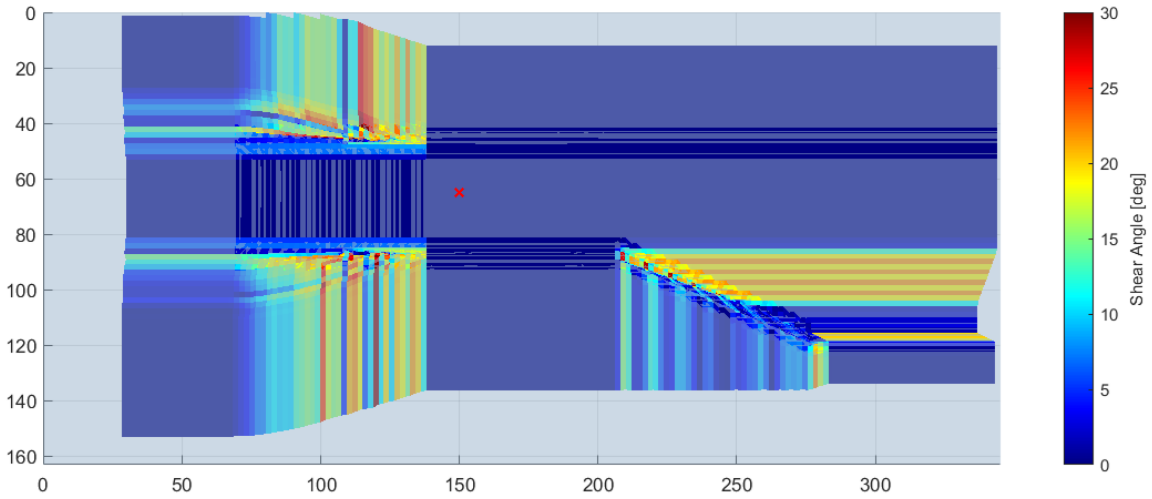

Figure 5: Shear Angle Distribution with IDP = [150,65] mm and Δd = 2mm

Kinematic draping was also performed using CATIA geodesic draping to assess the validity of the KinDrape results. Both simulations (Figure 6 & 7) show thick shear bands perpendicular to the tapered section [1] and thin bands extending parallel to the edges of the raised section [2]. They also show a thick shear band [3] and thin shear band [4] parallel to the bottom edge. They differ in magnitude, with KinDrape showing more variation of shear angle within the shear bands. CATIA simulated a mean shear angle of 5.1 degrees, compared to 4.7 degrees predicted by KinDrape.

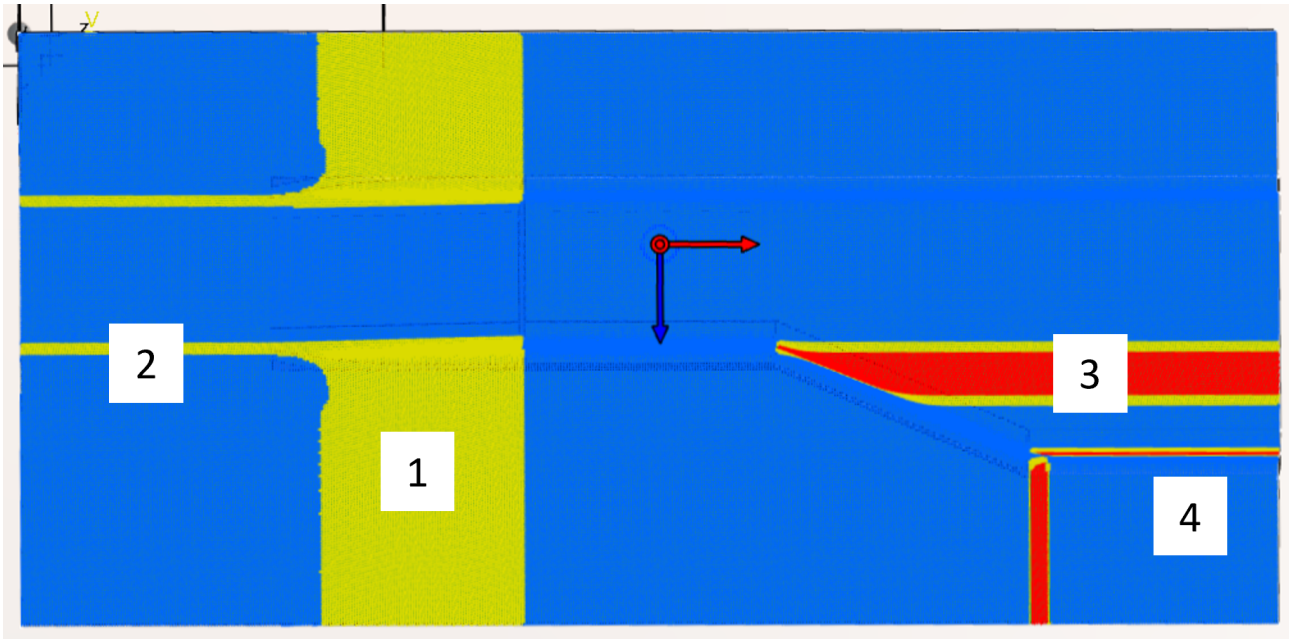

Figure 6: CATIA Geodesic Shear Angle Distribution: IDP = [150,65] mm, $\Delta d = 0.8$mm

CATIA was superior to KinDrape in terms of robustness, as it did not fail to produce results like KinDrape (Appendix A.3). CATIA also had superior resolution, as it calculated the shear angles for $\Delta d = 0.8$mm in around the same time KinDrape solved for $\Delta d = 2$mm. However, collecting and processing data from KinDrape was easier, as CATIA only shows shear angles in three bins ($< 10°$, $10° < \gamma < 20°$, $> 30°$).

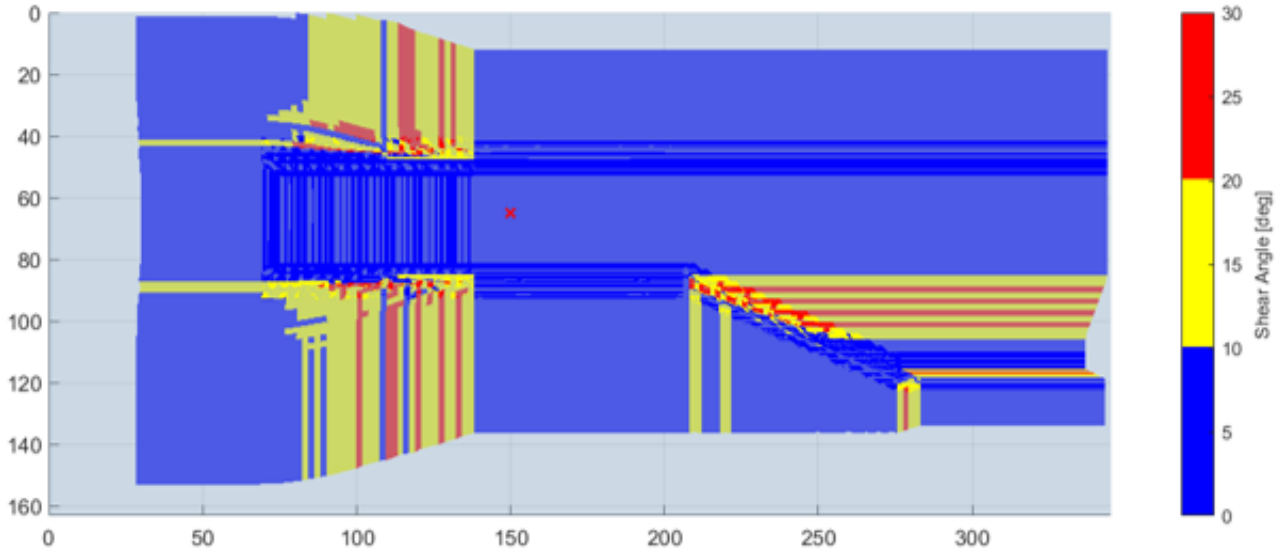

Figure 7: KinDrape Geodesic Shear Angle Distribution: IDP = [150,65] mm, $\Delta d = 2$mm

Overall, both KinDrape and CATIA produce similar shear distributions for the optimal IDP found through geodesic kinematic modelling. However, finite element analysis or experiments of the draping should be conducted to more accurately determine the magnitude of the shear angles, for resin infusion and structural optimisation calculations, due to the inherently conservative nature of kinematic draping.

3. Darts

Consider using darts to minimise the excessively sheared region (using Catia). Sketch the location of the darts and the changes in shear angle distribution caused by darting. Propose a design of darting in different plies of the preform to avoid fibre discontinuity. Consider implications of darting on fibre volume fraction in the affected region.

Since adding darts to the fabric does not affect the geodesic path, the optimised energy draping method was used in CATIA to assess the benefits of darts. This method generates new elements based on minimising the shear energy on the leading edge of the new element (Frommel & Körber, 2016). This gives a noticeably different shear angle distribution compared to geodesic draping, with mean of 6.6 degrees, showing the variability even within kinematic draping.

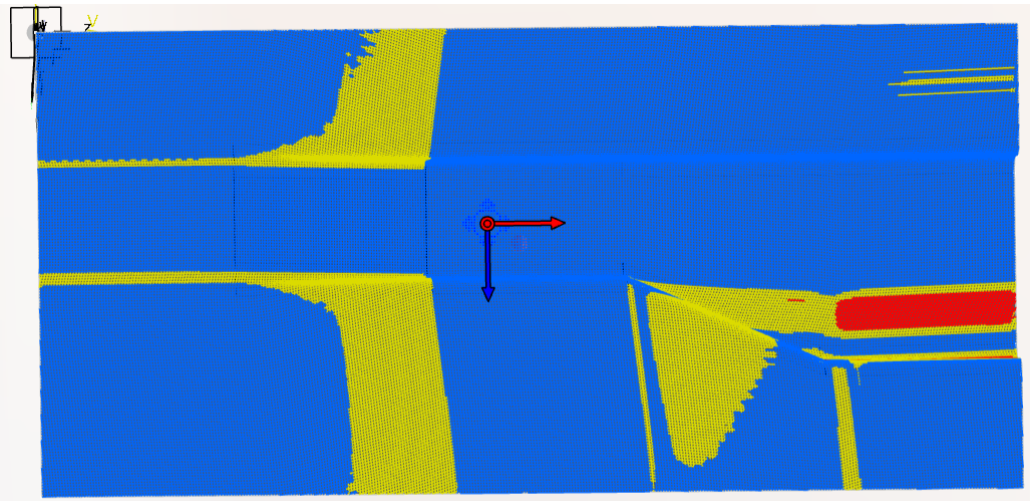

Figure 8: CATIA Optimised Energy Shear Angle Distribution at [150,65] mm

A dart was simulated through the region of greatest shear (Figure 9), so that the sheared region would redistribute itself around the free surface created by the dart. This reduced shear angles in the target region, but also increased the magnitude of shear angles within a different shear band [1]. Nonetheless, the addition of the dart was benficial, as it reduced the mean shear angle to 6.0 degrees and the maximum shear angle from 34.9 to 28.1 degrees.

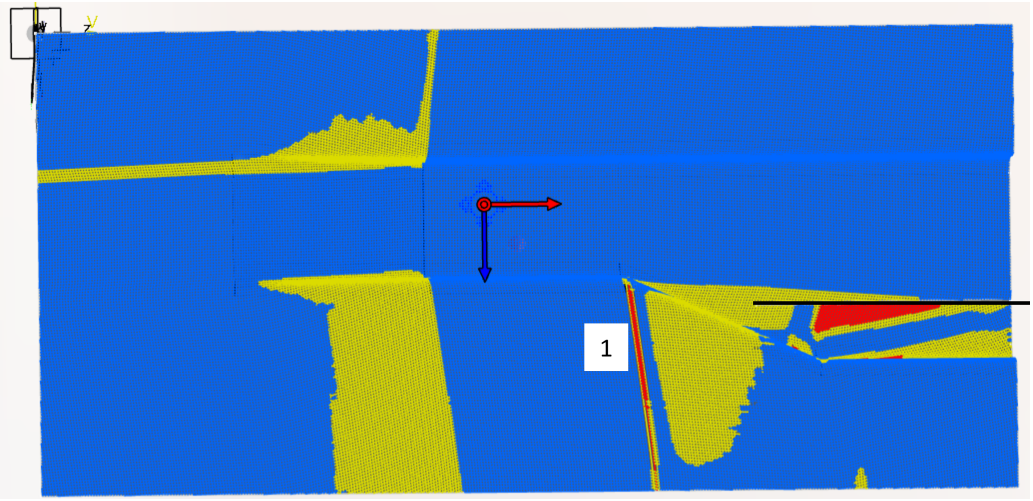

Figure 9: CATIA Optimised Energy Shear Angle Distribution with 1 dart

Following the same logic, another dart was placed in this new region of shearing (Figure 10). However, this only reduced the mean shear angle by 0.1 degrees, seemingly because the shear bands were redistributed back towards the original shear distribution [1]. Therefore, no more darts were implemented as they would only redistribute rather than reduce the shearing.

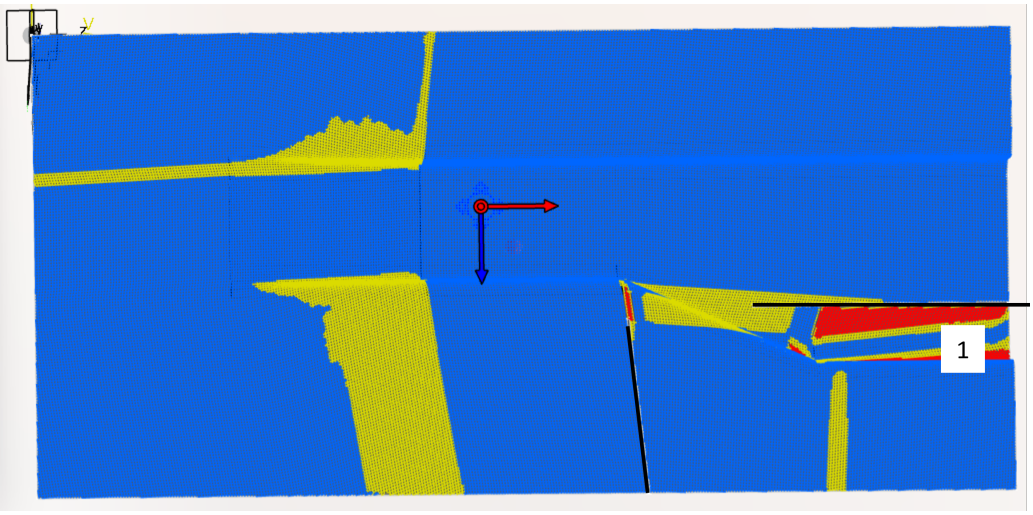

Figure 10: CATIA Optimised Energy Shear Angle Distribution with 2 darts

To avoid excessive fibre discontinuity, the two proposed darts should be implemented in different ply layers (Figure 11). Since the mechanical properties in the warp and weft directions may vary due to crimping (Xu et al., 2016), a typical layup for the floor panel may look like $[(0/90)_5]_s$, to mitigate this variation. This laminate is a symmetric meaning the coupling stiffness matrix **B** is zero (Nettles, 1994), which prevents twisting under the thermal stress applied during the curing process. It is also a balanced layup, having an equal number of 0° and 90° plies (Schenk, 2023), which results in zero extension-shear coupling, although these conditions are automatically satisfied if the warp and weft directions are identical. It is therefore proposed that the darting occurs in ply pairs, $[(A/A/B/B)_5]$, so that the dart is not cut solely along the warp or only along the weft direction.

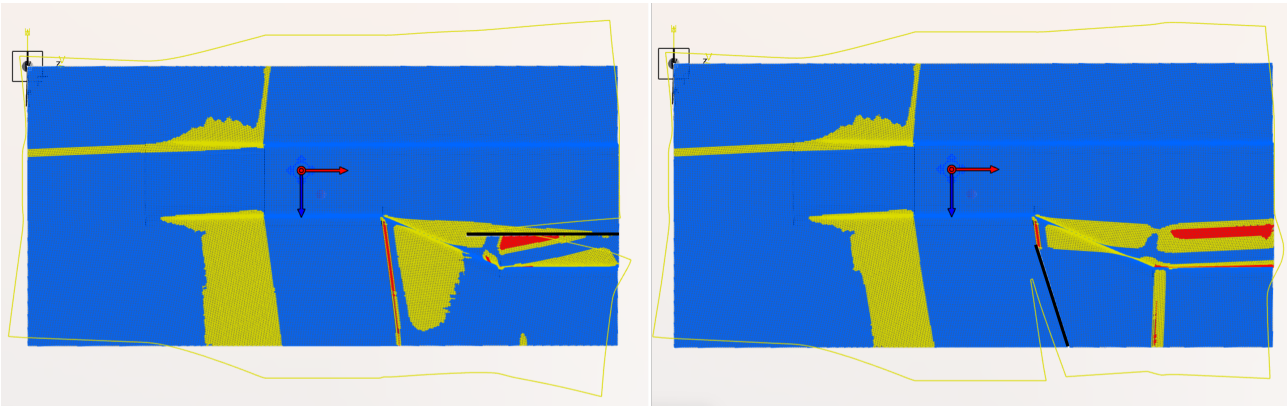

Figure 11: CATIA Optimised Energy Shear Angle Distribution - Ply A (L), Ply B (R)

However, implementing darts into the plies is a complex, manual task, and is therefore time intensive. This is not ideal for a vehicle floor panel, where high production throughput is essential. Additionally, the use of darts creates resin-rich zones within the ply that are inherently weaker than the non-darted regions (Skramstad, 1999). Finally, kinematic draping exaggerates the amount of shearing and therefore making darts seem more essential than in reality. Using a kinematic draping tool with finite element aspects such as FEFlatten in CATIA allows for longitudinal deformation of the fibre (Frommel & Körber, 2016), which is more representative

of the actual fibre behaviour. Using FEFlatten with two darts gives a much lower mean shear of 1.3° (Figure 12), albeit with a larger discretisation distance of 2mm to ensure reasonable computation time. At this low level of shear, darting itself causes shear concentration which defeats the purpose of the dart.

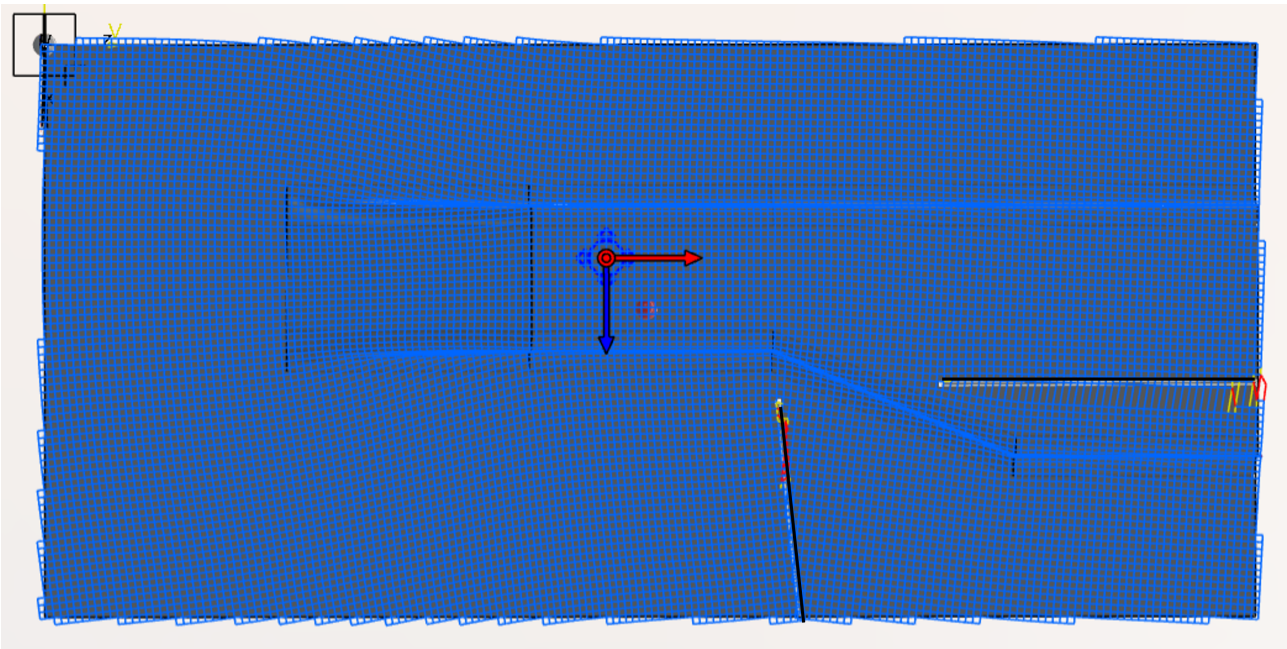

Figure 12: CATIA FEFlatten Shear Angle Distribution with 2 Darts

Therefore, for this application, the use of darts is not recommended. The floor panel does not produce large enough shear bands to warrant the use of darts, and creating darts is too time-consuming and labour-intensive for an automotive sector production line.

4. Injection Arrangement

Show the arrangements of vents, coils, injection gates aiming at complete filling of the cavity, minimisation of the fill time, and preventing impregnation defects. Calculate the characteristic flow length and infusion time taking into account drape deformations. Use the conservative estimate of permeability calculated in the most problematic drape region. Compare the conservative estimate of flow time if drape is not taken into account.

4.1 Characteristic Filling Time

The thickness of the laminate can be expressed using equation 3 (McIlhagger et al., 2020). To achieve a minimum fibre volume fraction of 50%, the thickness (h) of the cavity should be 8.3mm.

$$h = \frac{nA_w}{\rho_f V_{f,0}} \tag{3}$$

The fibre volume fraction can be related to the shear angle (Heardman et al., 2001). Taking the greatest shear angle from the most conservative draping simulation (35.5 degrees) gives a maximum fibre volume fraction of 61.4% (Equation 4).

$$V_f = \frac{V_{f,0}}{\cos(\gamma)} \tag{4}$$

The fibres must be compressed to achieve the nominal thickness, which in turn causes a stress between the fibres (Gutowski et al., 1987). Using the data provided in the coursework $\frac{3\pi E}{\beta^4} = 1.1$ Pa and $V_{f,max} = 0.75$, the compaction stress $\sigma(V_f)$ is 2.1 kPa (Equation 5). The resin pressure is the difference between the applied and compaction stress: $\Delta p_r = \Delta p - \sigma(V_f)$. To minimise infusion time (Equation 8c), the maximum feasible pressure difference should be used, which is 0.4 MPa with use of a vacuum pump. Therefore, the compaction stress is negligible compared to the total available pressure, giving a resin pressure of 398 kPa.

It should be noted the parameters used in Gutowski's original experiment ($\beta = 350$, $E = 234$ GPa) give a coefficient of $\frac{3\pi E}{\beta^4} = 147.0$ Pa. Using $V_{f,max} = 0.785$ for squarely packed fibres (Gutowski & Dillon, 1992) gives a compaction pressure of 120 kPa (Gutowski et al., 1987). This is much greater than provided in the coursework datasheet, and would have a significant impact on the resin pressure. Therefore, further studies should be conducted to determine the experimental compaction stress since it could have a major influence on the infusion time.

$$\sigma(V_f) = \frac{3\pi E}{\beta^4} \frac{\sqrt{\frac{V_f}{V_0}} - 1}{\left(\sqrt{\frac{V_{f,max}}{V_f}} - 1\right)^4} \tag{5}$$

The impact of fibre volume fraction on the permeability of a woven fabric can be described using the Kozeny-Carman relation (Appendix B.1). The effect of shearing on permeability can be described using equation 6 (Smith et al., 1997), giving the major and minor components of permeability at a shear angle of 35.5 degrees are 2.9e-13 and 0.9e-13 m^2 respectively (Figure 13).

$$K_1 = K_{||}\cos^2(\theta) + K_\perp \sin^2(\theta) - \frac{(K_{||} - K_\perp)^2 \sin^2(\theta)\cos^2(\theta)}{K_{||}\sin^2(\theta) + K_\perp \cos^2(\theta)} \tag{6a}$$

$$K_2 = K_{||}\sin^2(\theta) + K_\perp \cos^2(\theta) - \frac{(K_{||} - K_\perp)^2 \sin^2(\theta)\cos^2(\theta)}{K_{||}\cos^2(\theta) + K_\perp \sin^2(\theta)} \tag{6b}$$

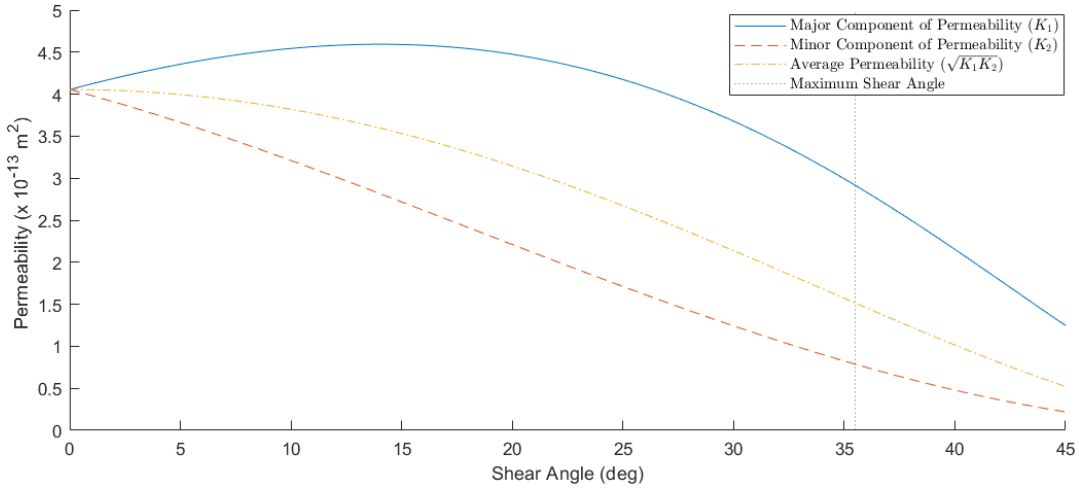

Figure 13: Permeability as a Function of Shear Angle (Equation 6)

These permeability values seem particularly low, considering the characteristic permeability of the preform is stated as being 0.2e-10 m^2. Smith also proposed an alternative equation in the same paper (Smith et al., 1997):

$$K_1 = K_{||} \cos^2(\theta) \tag{7a}$$

$$K_1 = K_{\perp} \cos^2(\theta) \tag{7b}$$

Which gives a non-sheared preform permeability of 0.205e-10 m^2 and a minor permeability (K_2) of **2.6e-12**m^2 at 35.5° (Figure 14). This agrees much more closely with the characteristic permeability stated in the coursework and published experimental results. For example, Demaría has experimentally tested the permeabilities of sheared, woven, carbon-fibre fabrics, observing that for $V_{f,0} = 45.7\%$ and $\gamma = 35°$, the minor permeability was 1.83e-11 m^2. Also, for $V_{f,0} = 57.1\%$ and $\gamma = 35°$ the minor permeability was recorded to be 3.67e-12 m^2 (Demaria et al., 2007)[1]. Another experiment for non-crimp fabrics gives $K_2 \approx$ 2e-12m^2 for $V_{f,0} = 46.4\%$ and $\gamma = 35°$ (Aranda et al., 2014)[2]. Therefore the estimated permeability of 2.6e-12 m^2 appears reasonable for a $V_{f,0} = 50\%$ and $\gamma = 35.5°$.

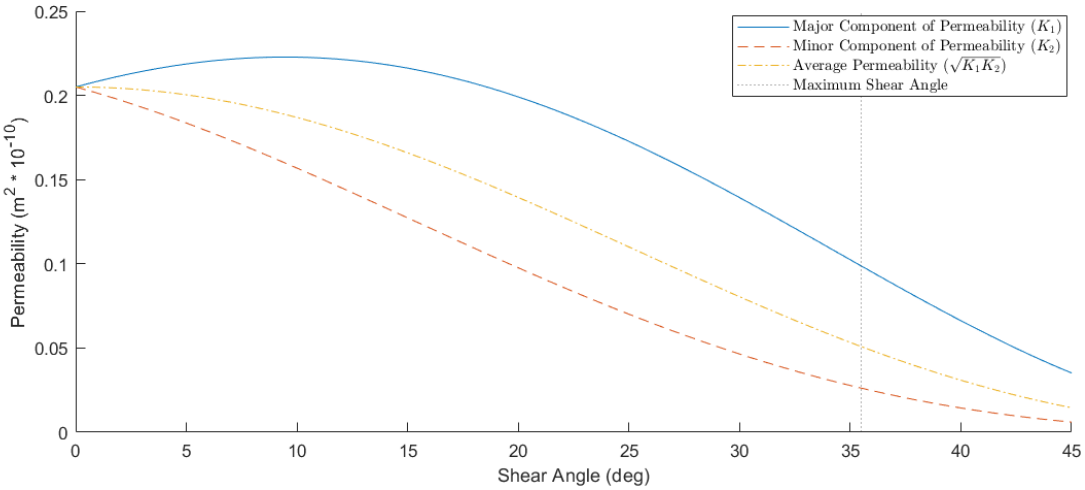

Figure 14: Permeability as a Function of Shear Angle (Equation 7)

[1]From Table 2 in *In-plane anisotropic permeability characterization of deformed woven fabrics by unidirectional injection*

[2]From Figure 6 in *Influence of shear on the permeability tensor and compaction behaviour of a non-crimp fabric*

4.2 Arrangement of Coils, Vents and Injection Gates

The objective of injection gate placement is to minimise infusion time, predominantly by minimising the flow length, to minimise energy costs and increase throughput. Using an injection gate allows the resin to radially flow out from the centre of the part (Figure 15), minimising the resin infusion time. Another requirement for the injection layout is to ensure thorough resin injection to minimise defects. Radial injection allows the injection process to be designed such that the resin only flows against gravity. This is beneficial as it prevents air bubbles becoming trapped and forming voids. However, placing an injection gate on the part would cause significant surface marking on the vehicle floor panel. Since the part is a vehicle floor panel, and likely to be seen by the customer, any markings are deemed to be unacceptable. However, this decision was based on the assumption that the composite floor panel is for a mid to high-end vehicle where the 2x2 twill fabric is visible for aesthetic purposes. If the floor panel is to be covered with a carpet then radial injection may be acceptable.

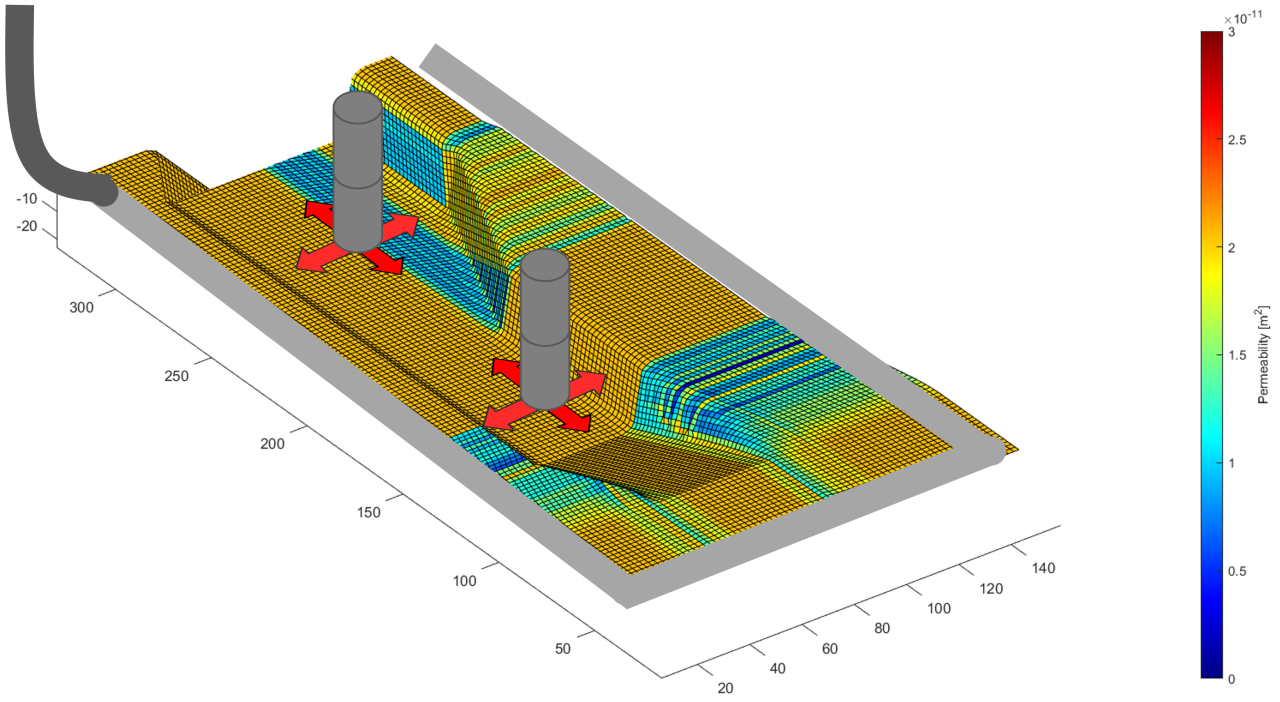

Figure 15: Layout of Coils, Vents and Injection Gates - Radial

Instead, linear injection (Figure 16) was preferred since it only causes markings on the edge of the part, which can be trimmed. The distance across the panel is 197mm (accounting for the change in elevation) and 358mm along the panel. To reduce the characteristic flow length, resin infusion across the panel[3] is preferred.

[3] An improved injection layout is proposed in section 5.2

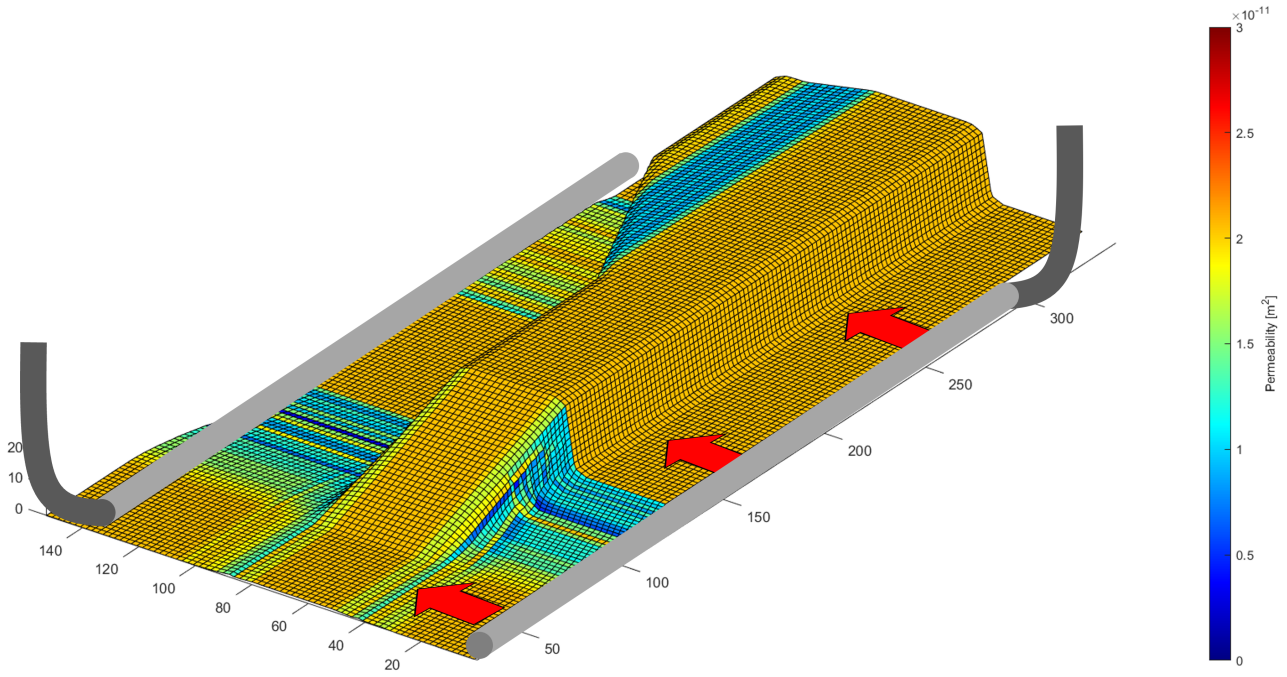

Figure 16: Layout of Coils, Vents and Injection Gates - Linear

The differential equation for 1D linear Darcy flow is shown in equation 8.

$$\frac{dx}{dt} = \frac{K\Delta p_r}{\mu(1-V_f)x} \tag{8a}$$

$$\int_0^L x\,dx = \int_0^{\Delta t} \frac{K\Delta p_r}{\mu(1-V_f)}dt \tag{8b}$$

$$\frac{L^2\mu(1-V_f)}{2K\Delta p_r} = \Delta t \tag{8c}$$

Substituting $L = 197$mm, $V_f = 0.614$ (Equation 4), $K_{\min} = 2.6$ x 10^{-12} m^2 and $p_r = 398$ kPa, the characteristic flow time is **17 minutes**. This is assuming a constant viscosity $\mu = 0.14$ Pa s, at a recommended injection temperature of 80° C (HexFlow, 2016). It is also assumed that there are no pressure losses due to friction in the injection pipe or hydrostatic effects due to the change in height. This time is unlikely to be accurate as the changes in viscosity with degree of cure and permeability with distance have not been considered. Nonetheless, it is useful to compare the infusion time without draping considerations ($K = 0.2$ x 10^{-10} m^2 , $V_f = 0.5$) which is just 3 minutes. Figure 17 shows the numerical solution to equation 8a.

4.3 Frictional Pressure Losses

Since the resin is only injected from one end of the coil, it will take a non-zero amount of time for it to reach the other end. The major force resisting the flow will be frictional pressure losses, as there are no hydrostatic effects since the coil is horizontal. This may cause uneven mould filling, since the fabric near the start of the coil will be more thoroughly impregnated than at the end.

$$\Delta p_r = \frac{1}{2}\rho\bar{u}_{coil}^2 + \Delta p_{loss} \tag{9}$$

The flow through the coil is assumed be laminar flow, giving a Darcy friction factor of $f = 64/\mathrm{Re}$. The diameter and length of the injection pipe are not known, so it assumed for simplicity

that $\Delta p_{loss,coil} = \Delta p_{loss,pipe}$. For the coil, L is 350mm, $\mu = 0.14$ Pa s and $D = 3$mm (Belnoue, 2023) giving $\Delta p_{loss} = 3.5\text{e}5\ \bar{u}_{coil}$. Substituting this into equation 9 and solving gives $\bar{u}_{coil} = 1.41$ m/s. Therefore characteristic time for the coil is 0.25s, negligible compared to the total fill time.

$$\Delta p_{loss} = \frac{1}{2}\rho \bar{u}^2 \frac{64}{\mathrm{Re}} \frac{L}{D} = 32\mu \left(\frac{\bar{u}_{coil} L_{coil}}{D_{coil}^2} + \frac{\bar{u}_{pipe} L_{pipe}}{D_{pipe}^2} \right) \approx 64\mu \left(\frac{\bar{u}_{coil} L_{coil}}{D_{coil}^2} \right) \tag{10}$$

This analysis can used to test the validity of assuming no frictional pipe losses in equation 8a. Taking the initial flow front x_0 as the radius of the coil (1.5mm), equation 8a gives the initial flow front velocity as 0.0127 m/s. Using conservation of mass:

$$\bar{u}_{coil} = \frac{A_{fibre}}{A_{coil}} \frac{dx}{dt} = \frac{hL_{coil}}{\pi D_{coil}^2/4} \frac{dx}{dt} \tag{11}$$

$\bar{u}_{coil}$ is 5.2 m/s. This cannot be true as the maximum coil velocity when considering frictional pressure losses is 1.41 m/s. However, this erroneous result only occurs when the flow distance x is small so that dx/dt is large. Therefore, it only increases the characteristic flow time by 1 minute for the maximum shear case (Figure 17). For the case where there is no shear, the effect of frictional losses is greater, since dx/dt is larger, which increases the flow time by 25%. Combining equation 8a and 10 gives equation 12, which is shown in figure 17.

$$\frac{dx}{dt} = \frac{\Delta p_r}{C_1 x + C_2} \tag{12a}$$

$$\text{where} \quad C_1 = \frac{\mu(1 - V_f)x}{K} \quad \text{and} \quad C_2 = \frac{64\mu L_{coil}}{D_{coil}^2} \left(\frac{4hL_{coil}}{\pi D_{coil}^2} \right) \tag{12b}$$

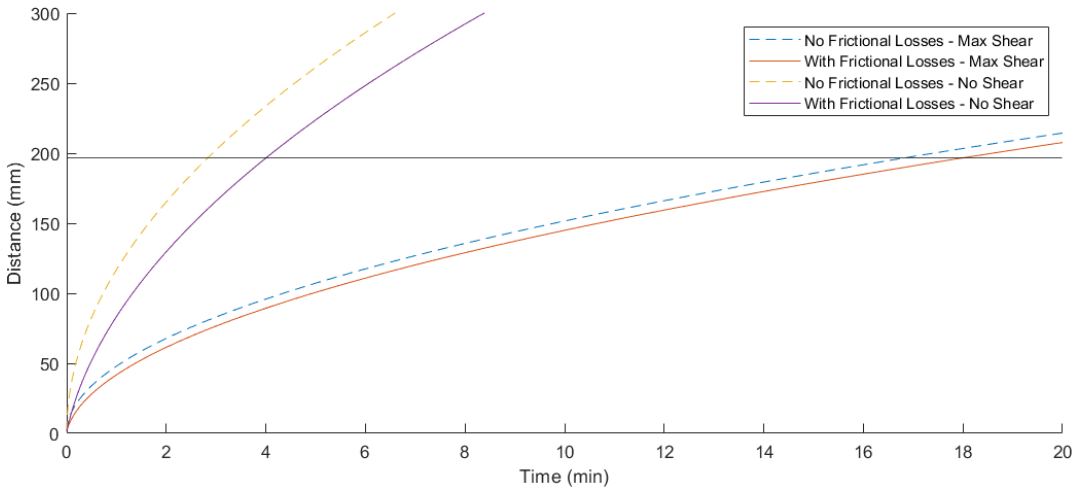

Figure 17: Impact of Frictional Losses in Coil and Pipe on Flow-front velocity

5. Flow Dynamics

Apply cure kinetics and rheological models (using coupled flow and cure tool in MatLab), choose infusion temperature to make sure that the mould is filled before resin. Show and discuss several options for infusion temperature (treat the termination of flow simulation due to excessively high viscosity as unsuccessful mould filling)

The optimum injection process will minimise voids and impregnation defects while reducing the time required to fill the mould to improve the production throughput. Ideally, once injection has finished, the resin will have homogeneous properties in all parts of the preform, to prevent defects occurring in cure, such as cure warpage. For automotive applications, cycle times of around 10 minutes (Verrey et al., 2006) are required to achieve the high volume of composite parts.

5.1 Injection Temperature Optimisation

Another factor to consider is the impact of degree of cure on viscosity. Using the chemorheological model provided in the coursework (Equation 13) and Darcy flow with frictional pipe losses (Equation 12), the coupled flow-cure equation can be solved.

$$\mu(\alpha, T) = \mu_{g0} \exp\left(\frac{-C_1(T - T_{g,0})}{C_2 + T - T_{g,0}}\right)\left(\frac{\alpha_g}{\alpha_g - \alpha}\right)^{A+B\alpha} \tag{13}$$

Using an infusion temperature of 80° C (Section 4.2), the mould filling time is 30 mins. This is likely due to a higher viscosity of 0.2 Pa s, which is a result of partial degree of cure. For an automotive composite part, this fill time too slow, as production throughput is essential.

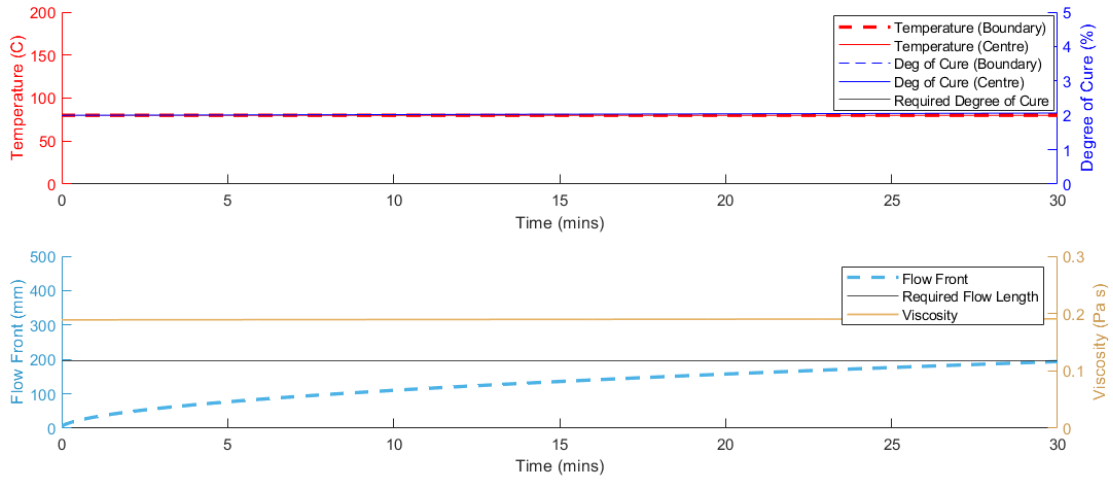

Figure 18: Cure and Flow for an Injection Temperature of 80° C

Using an injection temperature of 160° C reduces the mould filling time to just over a minute (Figure 18), a significant improvement compared to an 80° C injection temperature. However, injecting the resin at 160° C creates a risk that the resin cures if left too long in the pipes (Feigenblum & Senmartin, 2008). After 30 minutes at 160° C, the viscosity of the resin increases exponentially, which could lead to the pipes becoming blocked, which would cause costly disruption to the production line.

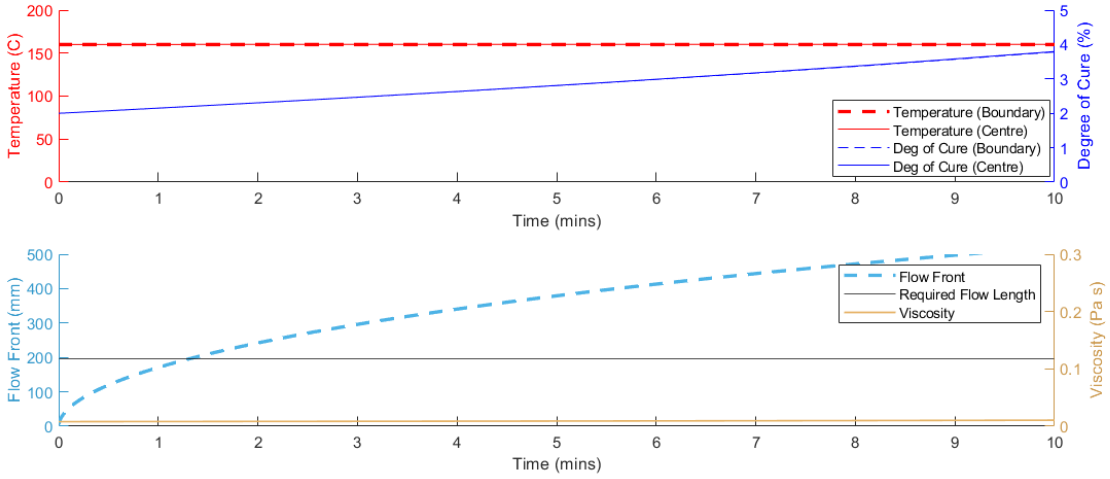

Figure 19: Cure and Flow for an Injection Temperature of 160° C

Therefore, the resin manufacturer Hexcel recommends to inject resin at **80**° C resin and pre-heat the mould to **120**° C (HexFlow, 2016). This gives a satisfactory fill time of around 5 minutes and prevents the resin curing in the pipe. However, the resin that is injected first will be heated to 120° C by the mould for the majority of the injection process and will therefore cure slightly more than the resin injected last at 80° C. However, the difference in degree of cure is only 0.1%, which is unlikely to have a significant impact on the overall cure. Also, the simulations contain many assumptions, whereas the manufacturer's recommended injection is likely to based on experimental data; therefore, following the manufacturer's guidelines ensure robustness against unknown factors that have not been implemented in the simulation.

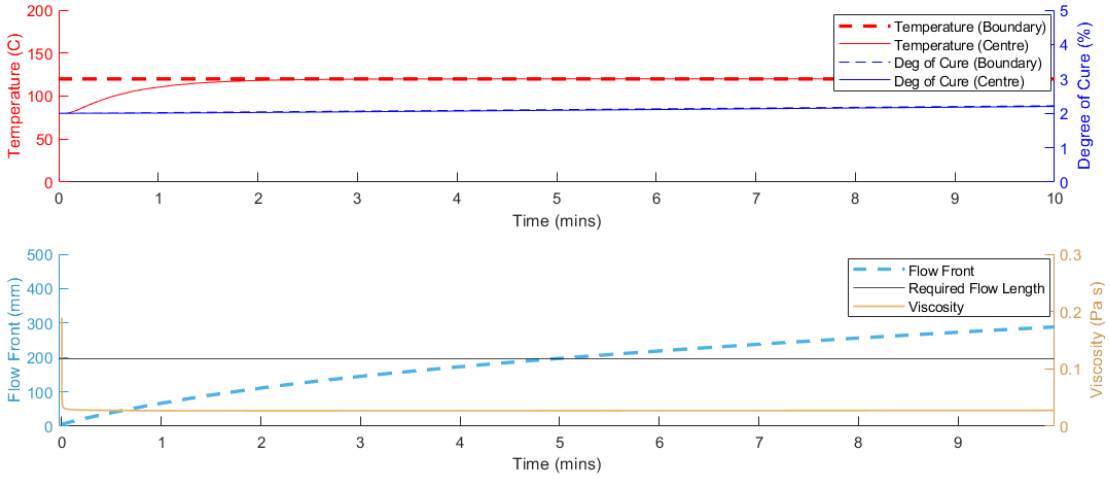

Figure 20: Cure and Flow for an Injection Temperature of 80° C, and Mould Temperature of 120° C

A map of the flow-front over time is shown in figure 21. It should be noted this is created by stacking together multiple 1D flows, so it does the permeability orthogonal to the direction of flow is zero ($K_2 = 0$). Even for a constant permeability of 2.6e-12 m^2 there is variability in the characteristic time as the flow length is greater over the raised section, leading to a 25mm difference in flow-front displacement. This is problematic as resin will start to be drawn through the vent at position [1] and into the vacuum generator, which would require the injection to be terminated to prevent damage occurring, without the entire part being impregnated [2]. Kinematic draping sometimes forces the elements off the surface of the part (Frommel & Körber, 2016) (Appendix C.1), which in turn increases the path length further [3] than path

length increase alone [2]. This is not realistic as the part is clamped at a constant thickness, and therefore the path length is constant, so the actual difference in flow front length could be lower.

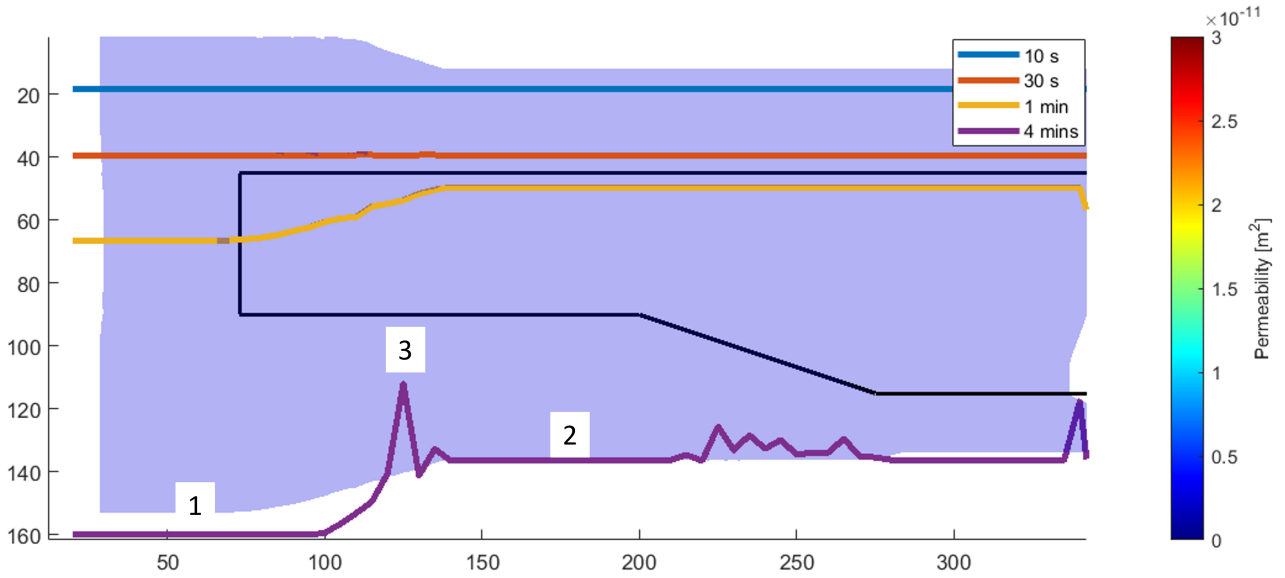

Figure 21: Flow Map for an Injection Temperature of 80° C, and Mould Temperature of 120° C with $\gamma = 35.5°$

On the other hand, figure 21 assumes a constant, conservative value for permeability (2.6e-12 m^2). Using the shear angle data from the KinDrape simulation (Appendix C.2), the effect of permeability can be evaluated. Since the permeability varies with shear angle the flow front lag is exacerbated (Figure 22), with a maximum difference of 68mm.

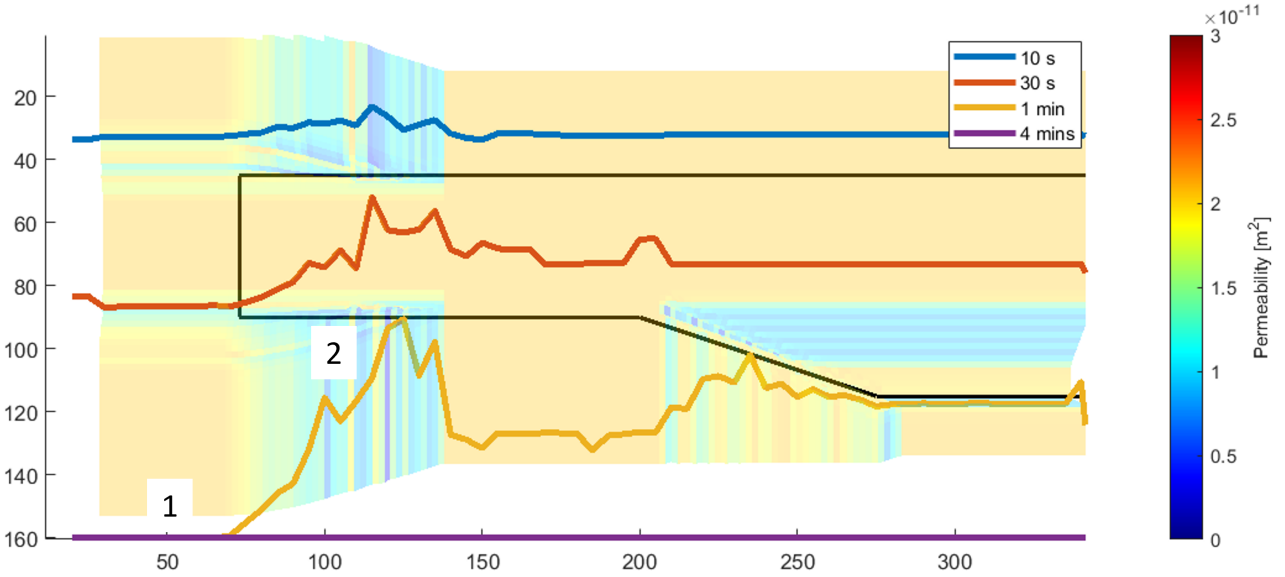

Figure 22: Flow Map for an Injection Temperature of 80° C, and Mould Temperature of 120° C

5.2 Updated Coil, Injection Gate and Vent Layout

To deal with this, the vent could be shortened (1) and moved to the other side of the part (Figure 23). Therefore once the flow has reached the end of the mould, it could still flow to fill any voids (green arrow). Another option is to increase move the coil further in the y-direction, and then trim the part to size. However, this increases the amount of waste and would also

require a larger mould. Alternatively, race tracking (2) could be implemented to encourage flow through a channel, which then disperses orthogonally into the most problematic region. Since race tracking will cause a resin-rich region and require increased complexity, moving the vent is preferred. It should also be re-iterated that in reality $K_2 \neq 0$, so the flow will permeate orthogonally to the direction of flow, smoothing the flow-front and reducing the variation in flow length.

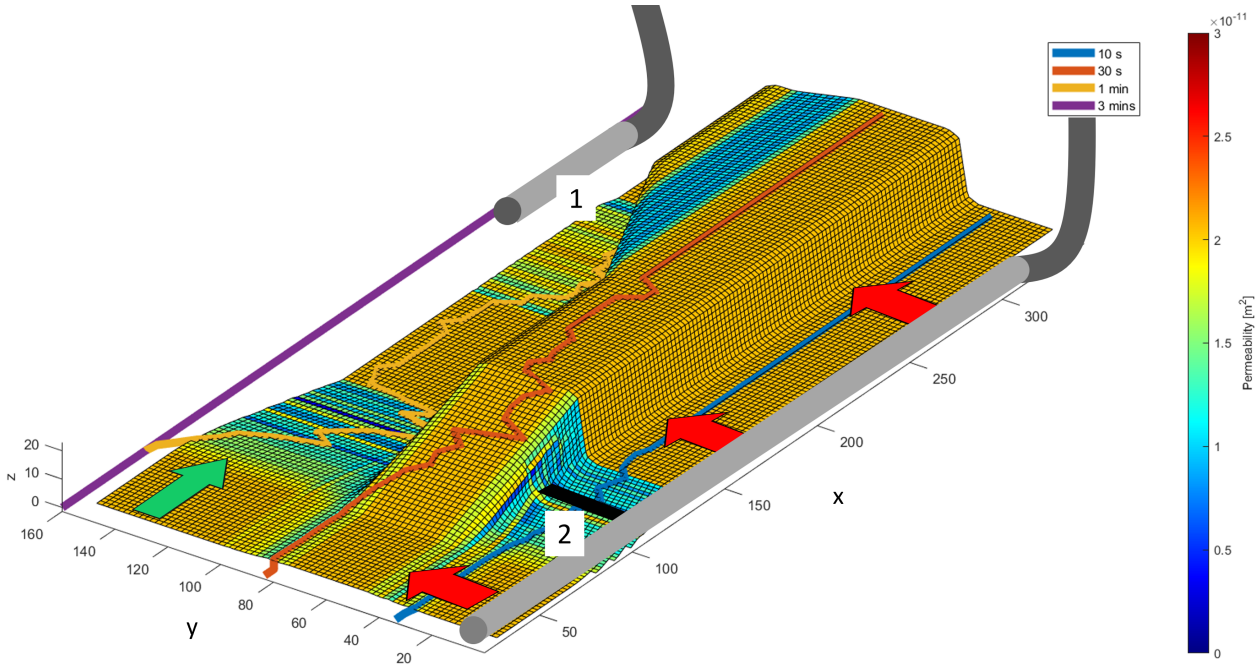

Figure 23: Updated Layout of Coils, Vents and Injection Gates

6. Heat Transfer

Suggest optimum cure cycle (using coupled heat transfer and cure tool in MatLab). Show at least 5 different options for cure cycle and explain why the optimum cycle worked the best. Calculate characteristic cure time ensuring over 92.5% cure and under 5 degrees exotherm everywhere through-thickness of the part

Once the mould filling process is complete, or near complete, the curing phase should begin (Advani, 1994). After injecting the resin at 80° C resin with a pre-heated mould, the datasheet (HexFlow, 2016) suggests a cure cycle of 120 minutes at 180° C (Figure 24). A ramp in temperature of 6° C / min and a cooling period of 20 minutes is added to represent a realistic heating and cooling period. The temperature during cooling is assumed to follow an exponential decay $T = \exp(-At)$. The simulation suggests this amount of curing is more than adequate, as 99.9% cure is achieved compared to a minimum required degree of cure of 92.5%. Maximising the degree of cure ensures the properties, such as glass transition temperature and flexural strength of the resin are optimal (Fu et al., 2019). However, for an automotive application the requirement to ensure full degree of cure is less stringent, as the component may not be placed under as severe loading conditions compared to the aerospace industry. Additionally, the maximum exotherm is 5.1 ° C, greater than the 5° C limit. Minimising the temperature overshoot helps to reduce strains due to thermal expansion in the curing process (Wang et al., 2023).

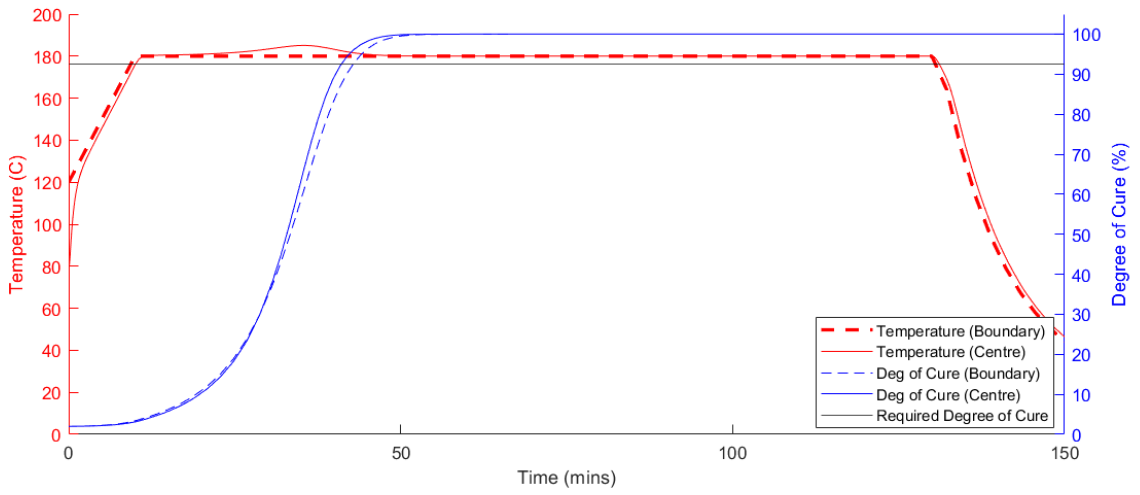

Figure 24: Cure Cycle v1 (Manufacturer Recommended)

Even by reducing the cure time from 120 minutes to 30 minutes, a 92.5% cure can still be achieved. However, the degree of cure is only 85% after 40 minutes, with the additional 7.5% cure occurring as the part cools. This means the degree of cure is very sensitive to the rate of cooling at the end of the cure cycle. Also, the exotherm is still an unacceptable 5.1° C.

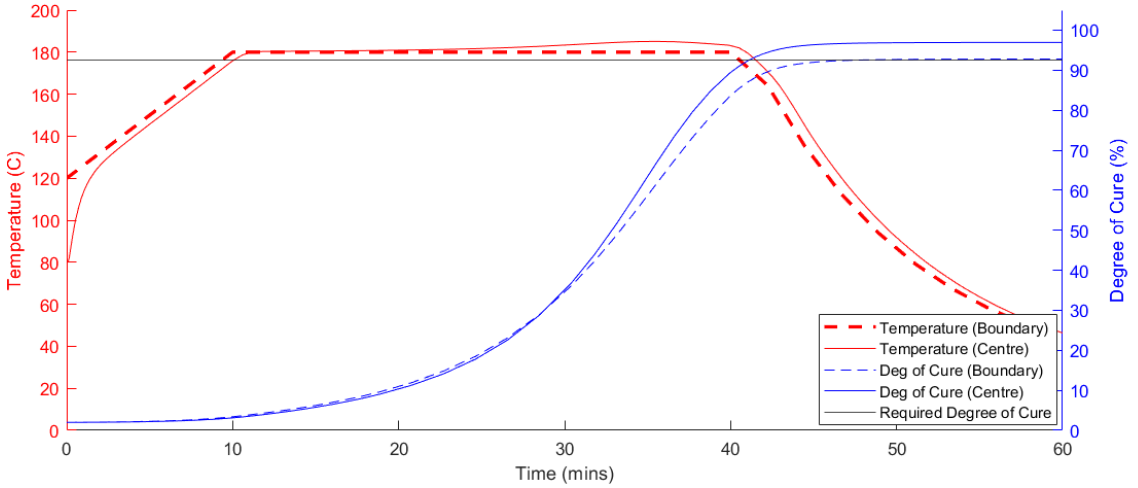

Figure 25: Cure Cycle v2

By introducing an initial dwell period, the exotherm can be timed to occur in the second ramp stage. Figure 26 shows a 7 minute ramp at 6° C/min, followed by a 47.5 minute dwell and a further 3 minute ramp to 180° C. This achieves 95% cure before cooling, increasing to around 98% after cooling. The exotherm is 4.9° C, however the total cure time is nearly 50 minutes longer than Cure Cycle 2.

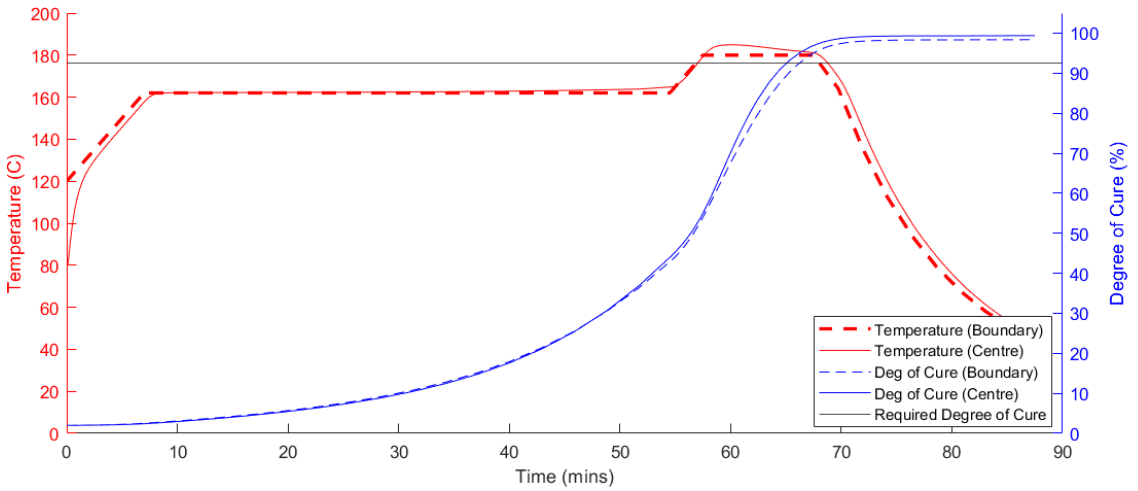

Figure 26: Cure Cycle v3

By increasing the temperature ramp speed, the optimum temperature can be achieved more quickly. The fastest practically achievable temperature rate for an RTM process is around 20°C/min (Karkanas & Partridge, 2000). By using a stochastic optimisation algorithm (Figure 27), the cure cycle can be reduced to just 39 minutes. The algorithm would vary either the first dwell time, second dwell time or first dwell temperature by a random value and compare to the previous iteration. If the new value had a lower or equal overall time, and the exotherm and degree of cure remained within the aforementioned limits, the new value was accepted. The range of possible random values decreased with the number of iterations to encourage convergence to a minimum. This was reasonably effective at returning an optimum cure cycle. However, the algorithm was quite sensitive to the initial input parameters, and due to the random nature of optimisation it never reached the same optimal cure cycle.

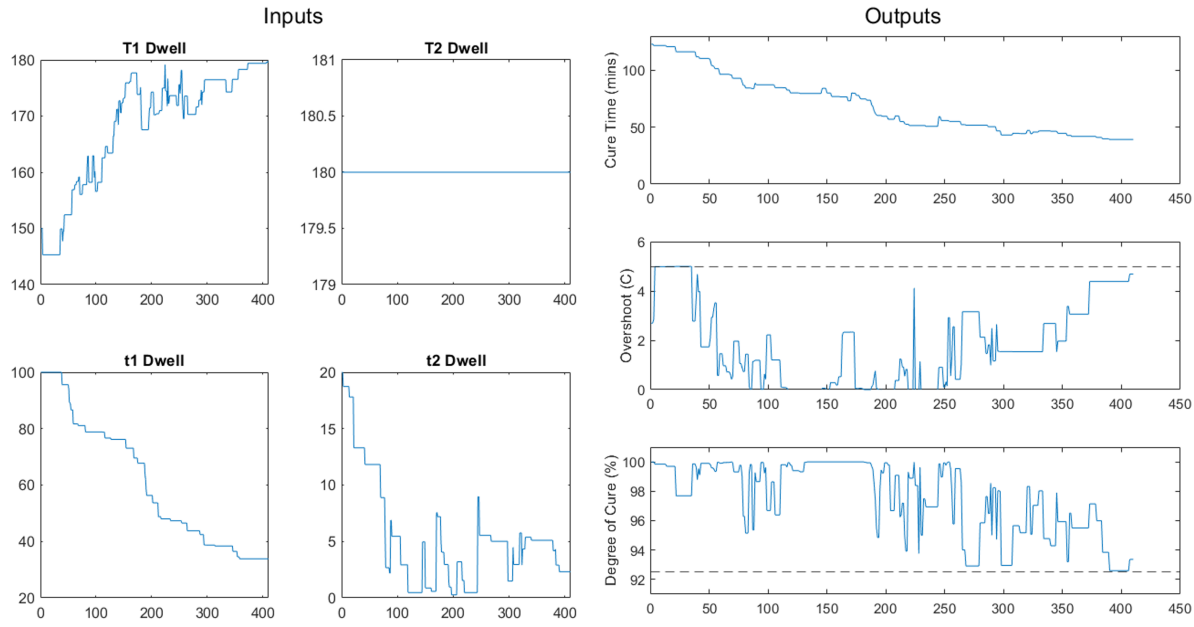

Figure 27: Optimisation for Cure Cycle v4

Cure Cycle v4 (Figure 28), has a 20°C/min ramp to 179.8°C with a 33 minute dwell. Another 20°C/min ramp to 180°C follows with a 3 minute dwell. This is very similar to Cure Cycle v2, because the exotherm was only 0.1°C over the limit, so only minor change is required. This leads to a 93.3% cure before cooling with an exotherm of 4.9°C. After cooling, this cure cycle is expected to achieve 95% to 98% degree of cure after a cooling time of 10 to 20 minutes.

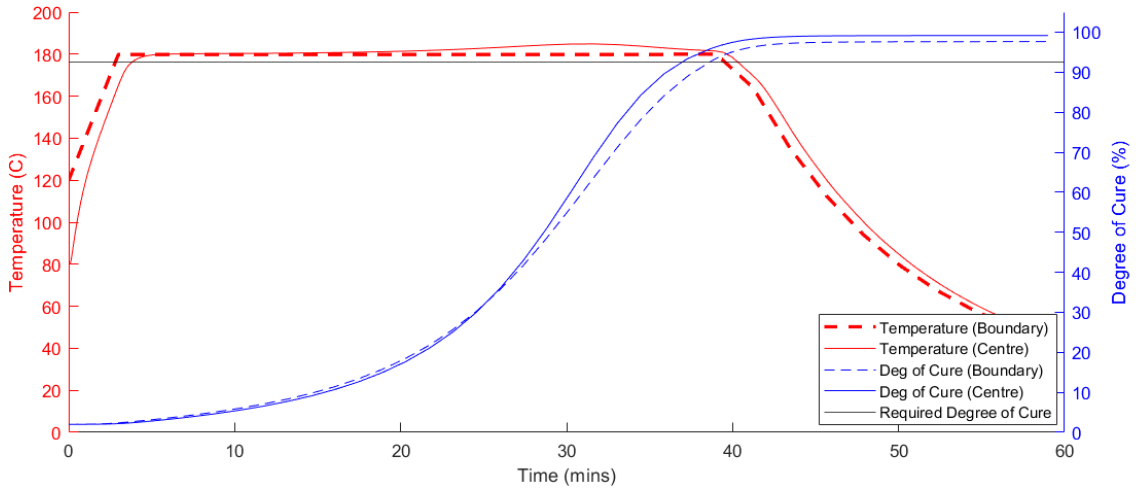

Figure 28: Cure Cycle v4

However, there is uncertainty surrounding the input parameters in the simulation. This means there is no safety margin applied in Cure Cycle v4, so any variation in parameters could lead to an unacceptable exotherm or degree of cure. In the exotherm limited case: +5% thickness, +5% cure rate, -5% specific heat capacity and -5% thermal conductivity, the exotherm of Cure Cycle v4 is 6.2°C. Additionally, in the cure-limited case, +5% thickness, -5% cure rate, +5% specific heat capacity and -5% thermal conductivity, the final degree of cure is 88.6% before cooling.

Instead, optimising for the cure-limited case gives a 177°C dwell for 34 minutes and a 180°C dwell for 7 minutes (Figure 29 & 30). This gives an exotherm of 3.2°C and a cure of 96.3% before cooling based on the original parameters. For the lower cure rate case, the exotherm is 4.3°C with a cure of 92.8%. Surprisingly, for the higher cure rate case, the exotherm is 2.7°C, however this is because the exotherm occurs during the first dwell, so the overshoot is actually 5.7°C but this is still acceptable, since it is below the 185°C limit.

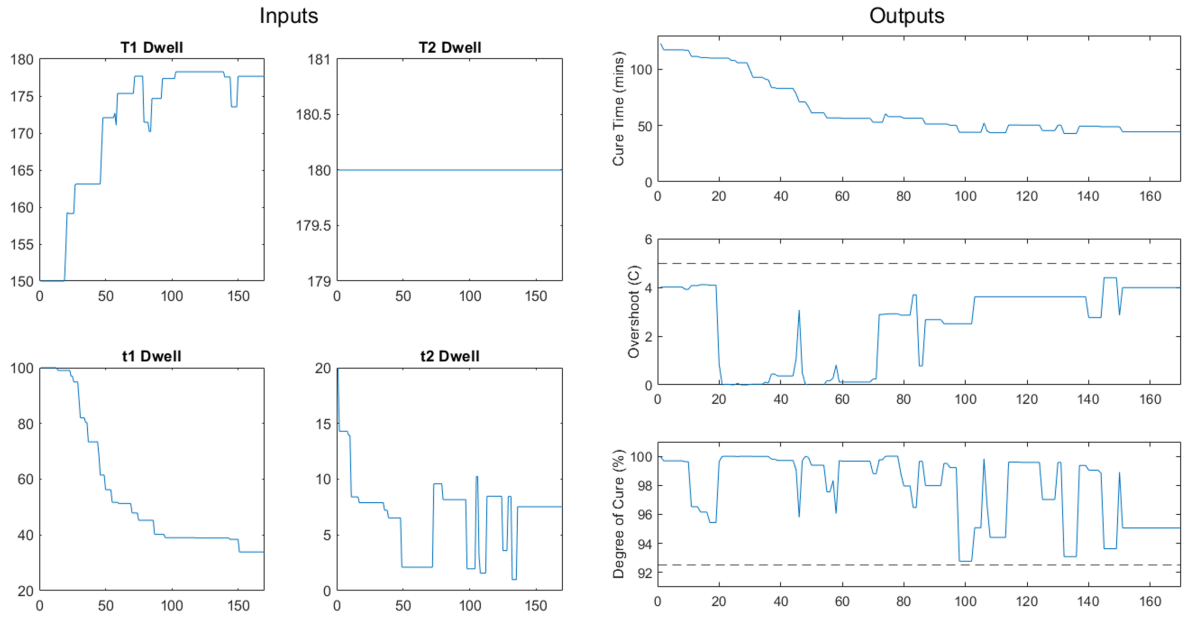

Figure 29: Optimisation for Cure Cycle v5 (-5% cure rate)

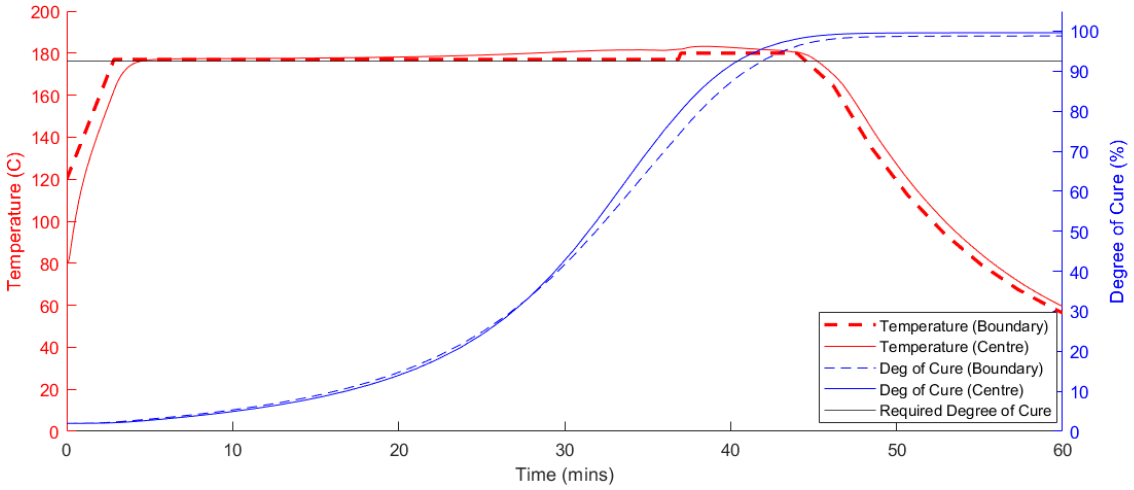

Figure 30: Cure Cycle v5

7. Requirements & Intellectual Property

The provided tool geometry shares similarities with the features found in a composite vehicle floor panel, typically manufactured using non-crimp fabrics (NCFs). Describe a set of potential functional requirements of a vehicle floor panel. Discuss the advantages and disadvantages of using NCFs over twill fabrics. Suggest a suitable tooling material, considering the RTM processing conditions. Conduct a patent search on any aspects of a composite vehicle floor panel (e.g., structural design, functionality, material, or manufacturing process, etc.) and describe the main novelty claimed.

7.1 Functional Requirements

The overall function of the vehicle floor panel is:

To protect the driver/passenger from the environment below the vehicle and to support the weight of the driver/passenger inside the vehicle

Without consulting with stakeholders over their individual needs, it is not possible to thoroughly define functional requirements, however reasonable, quantitative first guesses have been provided.

1) **Structural Integrity**

   1.1) Failure Criterion

      1.1.1) MUST not fail to a greater extent than any other part during a crash

      1.1.2) MUST be able to endure **>10,000** load cycles without failure
      Assume a user gets in and out once per day for 10 years = 7300 cycles

      1.1.3) MUST withstand the impact of debris at **70** mph

   1.2) Stiffness

      1.2.1) MUST not deflect more than **3** mm in any specified load case(s)

      1.2.2) SHOULD provide rigidity to vehicle's chassis

2) **Insulation from External Environment**

   2.1) Noise

      2.1.1) MUST not allow noise to exceed **80** dB in the vehicle when travelling at **70** mph
      Based on (Prasad et al., 2009)

      2.1.2) MUST prevent vibrations of more than **0.5**m/s^2 at **0.1-80** Hz
      Based on (Svantek, n.d.)

   2.2) Ingress

      2.2.1) MUST prevent ingress of liquids and dusts at **2** bar

   2.3) Thermal Insulation

      2.3.1) MUST prevent heat loss of more than **50** W/m^2
      Based on (Ruzic & Galamboš, 2017)

3) **Interfacing and Assembly**

   3.1) Assembly

3.1.1) MUST be able to interface or attach to other components e.g. chassis with standard joining components/methods

3.2) Conduit Systems

3.2.1) SHOULD allow wiring or piping to be embedded or attached

4) **Ergonomics**

4.1) Safety

4.1.1) MUST not have any sharp edges or other protruding features that could cause injury to the user

4.2) Comfort

4.2.1) MUST be not constrict the foot/leg movement for users in the 1^{st} - 99^{th} percentile of foot/leg size

7.2 Non-Crimp Fabrics

Crimp occurs in twill fabrics because the fibres in the warp and weft directions are intertwined, which causes bending of the fibres. This means only a fraction of all the fibres will be orientated in the principal fibre direction; therefore, it will have lower in-plane strength and stiffness (Vallons, 2015). Non-crimp fabrics (NCFs) are fabrics that consist of multiple, differently oriented layers of unidirectional (UD) fibres which are stitched together with a thin thread, preventing crimping to obtain a higher strength and stiffness. However, crimp increases the formability of the fabric making NCFs more difficult to drape. Additionally, NCFs display inferior impact resistance to twill fabrics (Sasikumar et al., 2019).

However, the piercing of the UD fibres during the stitching process produces local defects which can cause damage to the fibres and localised resin rich areas. On the other hand, these local defects form channels which can improve permeability and facilitate shear which can improve drapability (Vallons, 2015). Additionally, since the fibres are not woven through each other, fibre locking cannot occur, leading to reduced wrinkling in NCFs (Loendersloot, 2011).

Twill fabrics tend to experience 'nesting', the process by which multiple stacked layers tend to deform into each other, decreasing the thickness per layer with an increasing number of layers under a given pressure (Lomov et al., 2003). This leads to variability in the properties of the laminate, such as permeability, which makes designing and manufacturing the laminate more challenging. NCFs lie flat on each other, so do not experience this nesting problem.

7.3 Tooling

The function of composite tooling is to be a fixed surface which the composite is pressed to. One of the most important parameters is the coefficient of thermal expansion (CTE) of the tool. The difference between the CTE for the tool and part determines the dimensional error due to expansion.

$$\Delta L = L(\text{CTE}_{part} - \text{CTE}_{tool})(T_{gel} - T_{amb}) \tag{14}$$

The thickness of the tool depends on the design and loading scenario, but it can be simplified to a loaded plate (Engineer's Edge, n.d.), with the following scenario based on a maximum permissible deflection (δ) of 1mm (Equation 15a).

$$\delta = \frac{0.142pa^4}{Et^3(2.21(a/b)^3 + 1)} \tag{15a}$$

$$m = \rho abt, \text{ energy} = c_p m, \text{ cost} = Cm \tag{15b}$$

Comparing the difference in CTE between the part and tool and the thermal energy of the part gives titanium and Invar 36 as the optimal materials (Figure 31). However, when the raw material cost is factored in, aluminium and steel perform better (Figure 32). The exact values for thermal energy and cost are likely to be significant underestimates as they do not consider the shape of the tool, heat losses, manufacturing costs etc, but they can be used to compare between values. Since this is an floor plate for automotive applications, the dimensional tolerances may be less stringent than for aerospace applications, so a cheaper material with a higher CTE is preferable. Assuming the cost of industrial electricity is 28p per kWh (Department for Energy Security & Net Zero, 2023), after 1,000 cycles both aluminium and low carbon steel are predicted to have a combined material and energy cost £800. Assuming the labour costs are the same for steel and aluminium, low carbon steel should be used if the number of parts to be produced off the tool is expected to exceed 1,000, otherwise aluminium should be used.

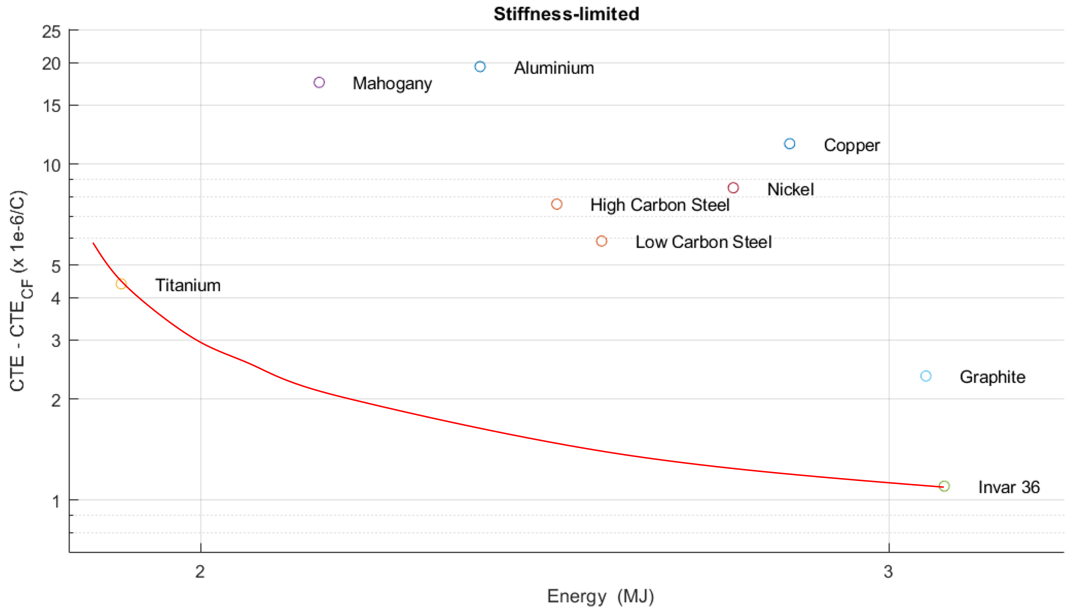

Figure 31: Material Selection Chart (Energy vs CTE)

However the material selction decision is based off limited analysis. The cost analysis assumes the labour, manufacturing or transportation costs associated with creating the tool are proportional to the raw material cost. It also assumes a stiffness-limited design, whereas the

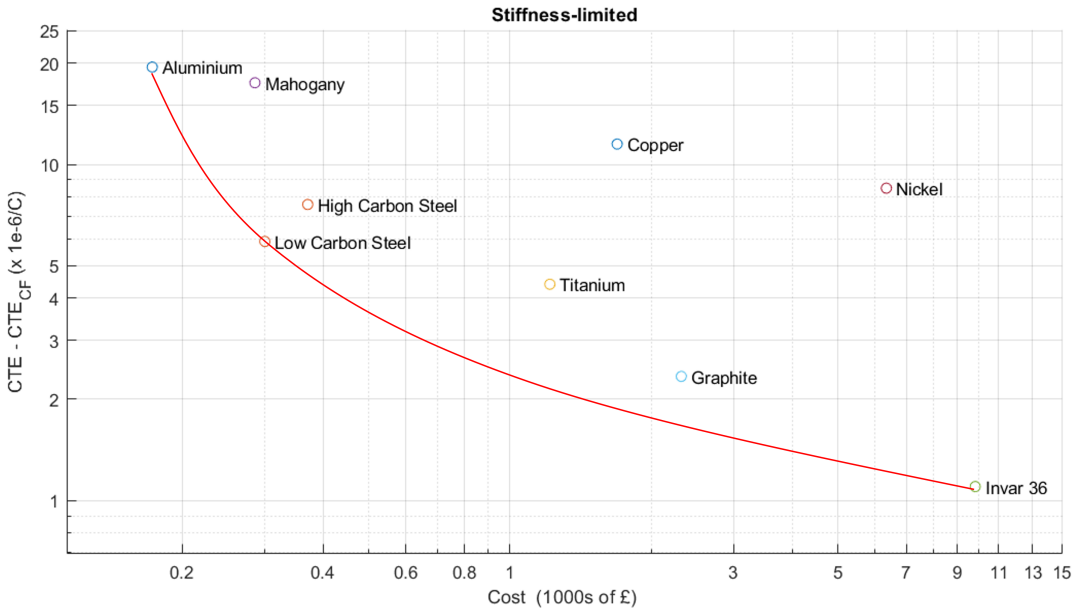

Figure 32: Material Selection Chart (Cost vs CTE)

actual design could be strength limited. Finally, the expected life of the tool is assumed to be constant for all materials. However, some materials may be more durable than others, and therefore cheaper in the long-term as they do not need to be repaired or replaced.

7.4 Intellectual Property Search

Patent EP 3 357 796 B1 (Santoni, 2019), is a patent for a novel method of joining the roof of a vehicle to a composite tub using adhesives, submitted by the proprietor McLaren Automotive Ltd to the European Patent Office. Modern luxury, sports cars do not have individual floor panels but entire monocoque tubs. Despite this, potential methods of joining the floor panel previously analysed could require a similar joining process, and consequently infringe on this patent. Currently, the joining process involves a large mass of adhesive which is detrimental to the mass of the vehicle and also requires considerable machining to achieve the desired tolerances which increases labour costs. Additionally, the current process does not facilitate undercuts in the design of the tub, minimising the design choice.

The independent claim in this patent is a method to join two parts. The 'first body' (i.e. the tub) which is formed in a 'rigid state' (i.e. by an RTM process). A mould is then formed over this part to secure the 'second body' (i.e. the roof) to the 'first body', and coupled together, followed by the application of pressure and temperature for 'rigidifying the precursor material', (i.e. curing the resin). In-between the first and second bodies, there is a 'flexible zone' to allow the joint to expand and contract instead of requiring machining to achieve desired tolerances. It should be noted how general this statement is, only referring to two bodies, a 'precursor material' and a 'flexible' and 'rigid' zone; therefore, the independent claim is applicable to many joining processes outside of composite manufacturing. The scope of the claim is iteratively narrowed with dependent claims . In claim 7, the patent specifies the 'precursor material' comprising of 'a resin matrix and a reinforcing component' and in claim 4 the 'flexible zone' is to comprise of multiple 'flexible plates'. Claim 9 states an 'inflatable flexible bag' is used to apply pressure on the inside of the two parts to facilitate the curing process. The other claims relate to specifics of the process, claims 2 and 3 state the flexible and rigid zone are attached together and at the interface between the first and second body. Claims 5 and 6 relate to a free, tapering of the composite laminate and claim 8 relates to the resin being in contact with

the body during curing (Figure 33).

The novelty of this design is limited, with nine existing inventions cited by the patent examiner. For example, a process of attaching the body to the roof of a car was patented by Ford in 1970 (Thomson Jr., 1970). This involved the use of adhesives to bond plastic pieces to protect the interface between the metal body and roof from corrosion. Also, a process of curing a new part onto a pre-existing component is not novel, with a patent filed by the German Aerospace Center in 1995 (Pabsch, 1997). Coupling multiple moulds is also not novel with Lamborghini spA patenting a way of mechanically fastening multiple moulds together (Masini, 2017). The novelty of the patent is generated by the application of similar existing ideas to a composite automotive vehicle, and also in the specificity of the claims in the patent, which only cover a narrow scope of design when the dependent claims are introduced.

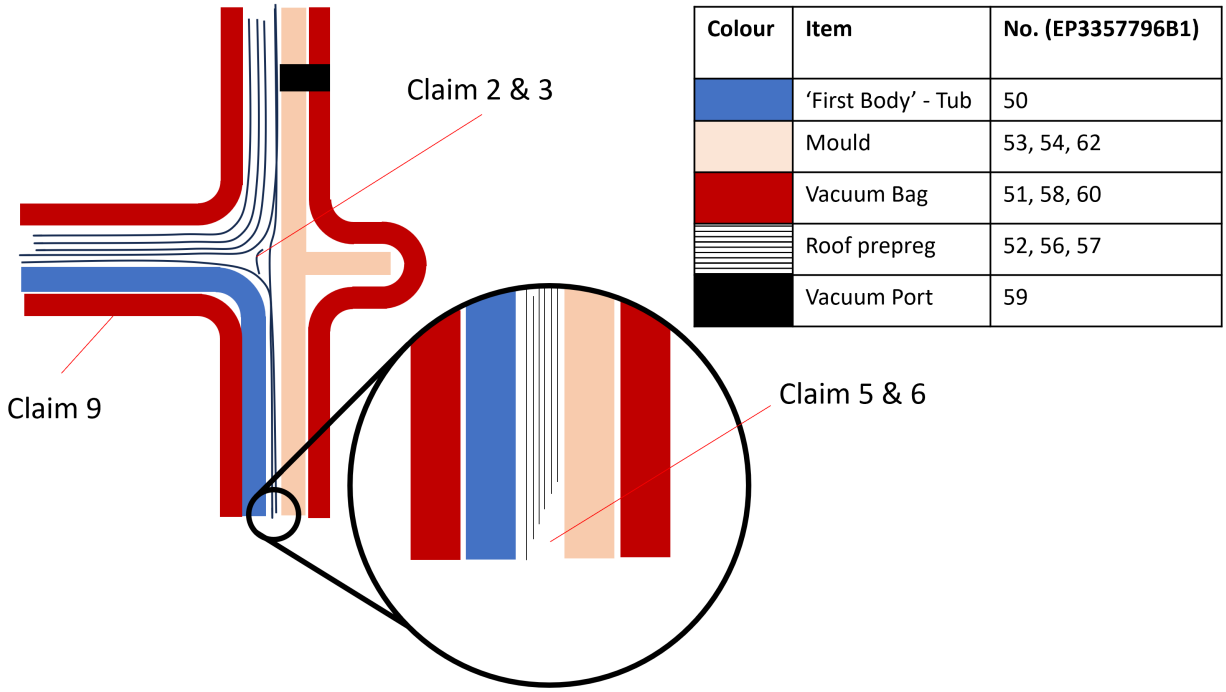

Colour	Item	No. (EP3357796B1)
	'First Body' - Tub	50
	Mould	53, 54, 62
	Vacuum Bag	51, 58, 60
	Roof prepreg	52, 56, 57
	Vacuum Port	59

Figure 33: Diagram of EP3357796B1

Interestingly, the patent also lays claim to certain aspects of the RTM process such as an injection temperature 25-70 deg C, injection pressure 1.5-2.5 bar and tool opening temperature of 40° to 70° C for a 2x2 twill or plain weave fabric. This may have implications for McLaren as a competitor has rights over a process which may be optimal any composite parts that McLaren design. Fortunately, the manufacturing process stated previously does not infringe on Lamborghini's patent, for the injection temperature of 80 deg C and injection pressure of 4 bar but it is possible there is already a patent that does claim similar RTM process parameters. This would necessitate changing the manufacturing process to avoid infringement, paying a fee to use the process or to buy the patent from the assignee.

Appendices

A. Draping

A.1 Optimum Initial Draping Regions

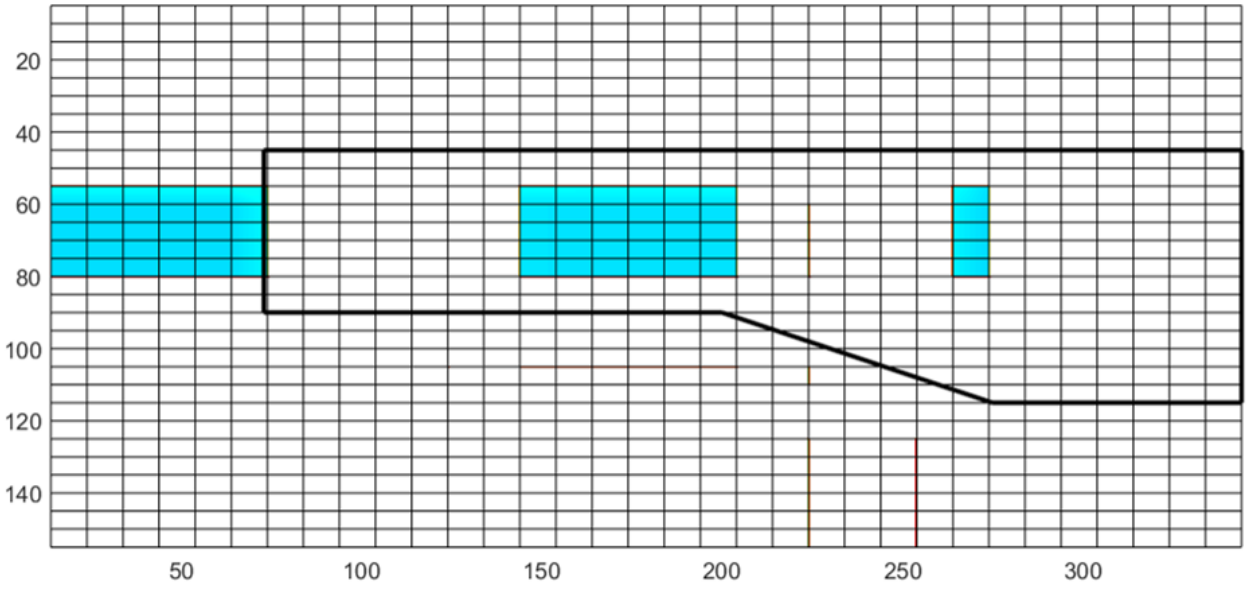

Figure 34: Optimum Initial Draping Positions with $\bar{\gamma}$ threshold (Figure 2)

A.2 Sketch of Shear Bands

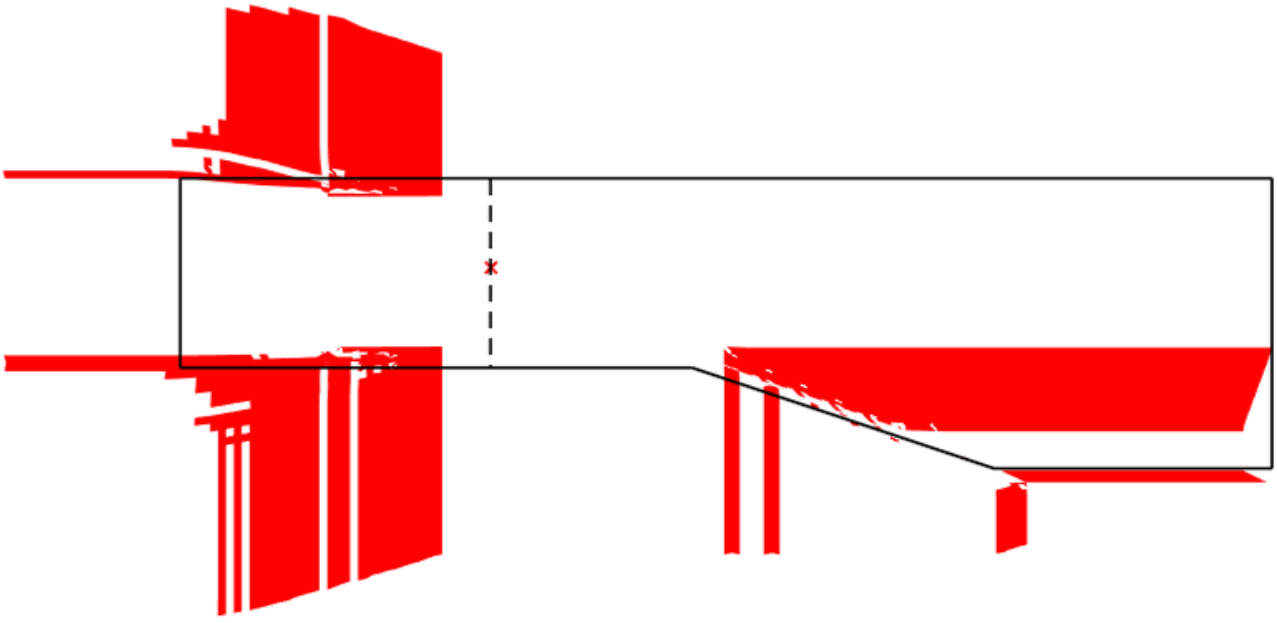

Figure 35: Sketch of the Shear Bands

A.3 Fabric Coverage after Draping

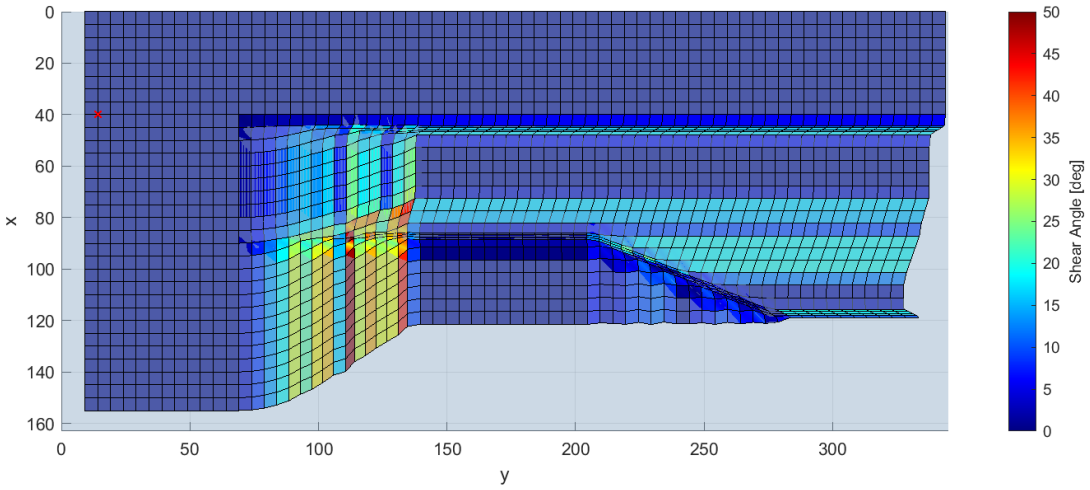

Figure 36: Shear Angle from an Initial Draping Position of [15, 40] mm

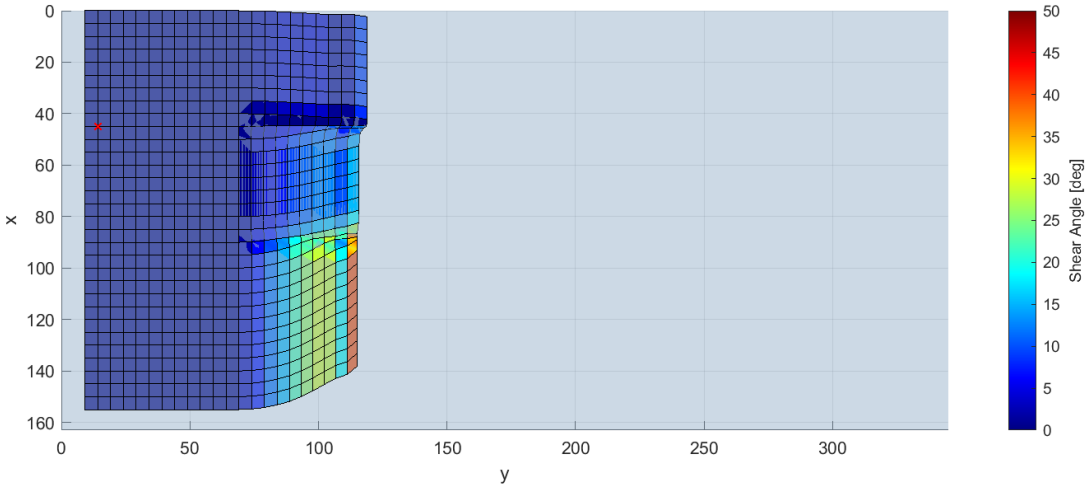

Figure 37: Shear Angle from an Initial Draping Position of [15, 45] mm

B. Vents & Coil Arrangement

B.1 Impact of Fibre Volume Fraction on Permeability

The Kozeny-Carman relation, originally developed for laminar flow through granular beds, can be used to describe the permeability of composite fabrics in the longitudinal direction (Smith et al., 1997).The value of $C_{||}$ is 0.82e-10 m^2 for this composite.

$$K_{||} = C_{||} \frac{1 - V_f^2}{V_f^3} \tag{16}$$

Additionally, the permeability in the transverse direction can be described by equation 17 for squarely packed fibres (Gebart, 1992).

$$K_{\perp} = C_{\perp} \left(\sqrt{\frac{V_{f,max}}{V_f}} - 1 \right)^{5/2} R^2 \quad \text{where } C_{\perp} = \frac{16}{9\pi\sqrt{2}} \tag{17}$$

C. Flow Dynamics

C.1 Lifting of Nodes off the Surface of the Part

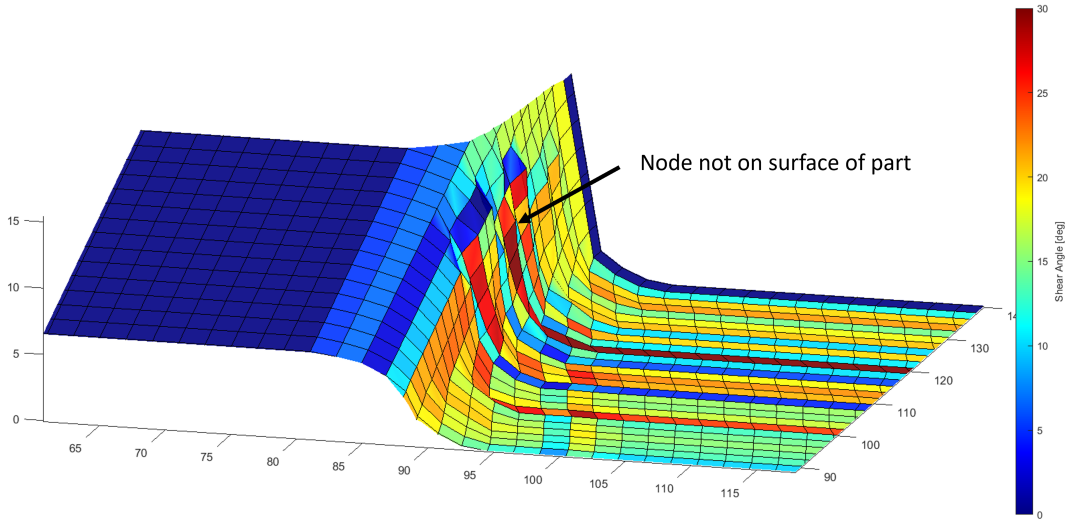

Figure 38: Lifting of Nodes off the Surface of the Mould

C.2 Bilinear Interpolation

The shear angle within a mesh element can be described as:

$$f(x, y) = a + bx + cy + dxy \tag{18}$$

Which can be expressed in matrix form as:

$$\begin{bmatrix} A_1 \\ A_2 \\ A_3 \\ A_4 \end{bmatrix} = \begin{bmatrix} 1 & x_1 & y_1 & x_1 & y_1 \\ 1 & x_2 & y_2 & x_2 & y_2 \\ 1 & x_3 & y_3 & x_3 & y_3 \\ 1 & x_4 & y_4 & x_4 & y_4 \end{bmatrix} \begin{bmatrix} a \\ b \\ c \\ d \end{bmatrix} \tag{19}$$

Solving this along a planar path over the composite gives (Figure 39).

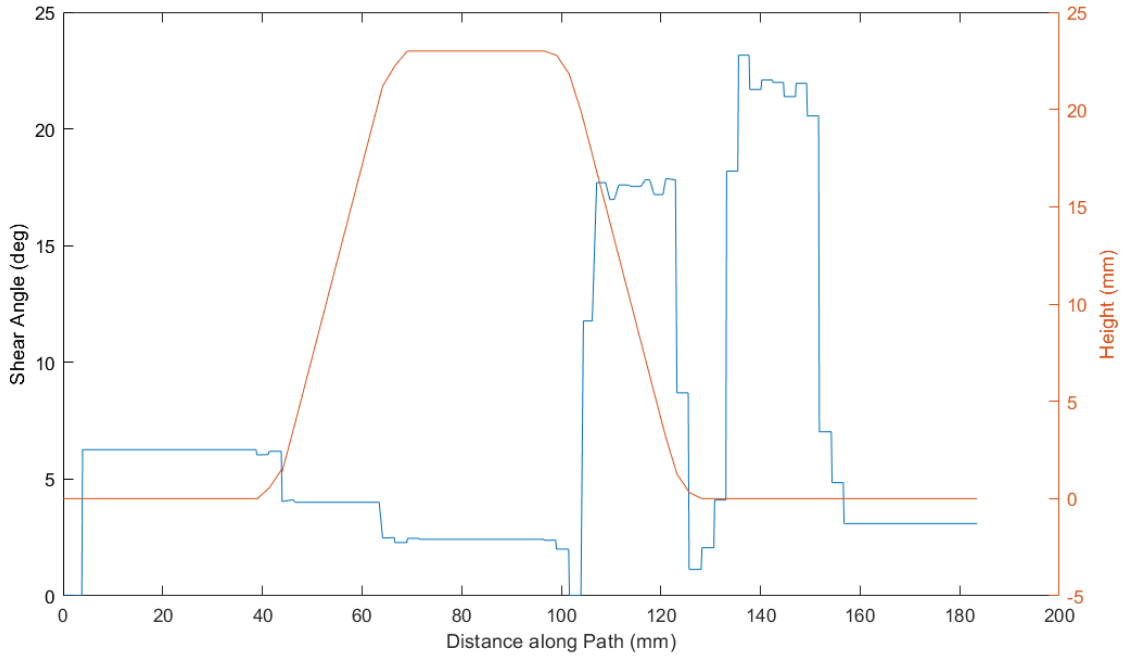

Figure 39: Shear Angle and Height along Flow Path

References

Advani, S. G. (Ed.). (1994). *Flow and rheology in polymer composites manufacturing* (Vol. 10). Elsevier.

Aranda, S., Berg, D., Dickert, M., Drechsel, M., & Ziegmann, G. (2014). Influence of shear on the permeability tensor and compaction behaviour of a non-crimp fabric. *Composites Part B: Engineering*, *65*, 158-163. Retrieved from `https://www.sciencedirect.com/science/article/pii/S1359836814000821` (Damage Mechanics) doi: https://doi.org/10.1016/j.compositesb.2014.02.005

Belnoue, J. (2023). Tutorial. coupled flow and cure in liquid moulding..

Demaria, C., Ruiz, E., & Trochu, F. (2007). In-plane anisotropic permeability characterization of deformed woven fabrics by unidirectional injection. part i: Experimental results. *Polymer composites*, *28*(6), 797–811.

Department for Energy Security & Net Zero. (2023). *Prices of fuels purchased by non-domestic consumers in the united kingdom excluding/including ccl (qep 3.4.1 and 3.4.2).* Retrieved from `https://www.gov.uk/government/statistical-data-sets/gas-and-electricity-prices-in-the-non-domestic-sector`

Engineer's Edge. (n.d.). *Rectangular plate uniform load simply supported equations and calculator.* Retrieved from `https://www.engineersedge.com/material_science/rectangular_plate_uniform_load_13643.htm` (Accessed on 04/12/2023)

Feigenblum, J., & Senmartin, J. (2008). Rtm technology improvement with tool surface heating by induction. In *Proceedings of the 9th international conference on flow processes in composites materials (fpcm-9), montréal, qc, canada* (pp. 8–10).

Frommel, C., & Körber, M. (2016). Comparison of fibre angles between hand draped carbon fibres and draping simulation.

Fu, H., Qin, Y., He, X., Meng, X., Zhong, Y., & Zou, Z. (2019). Effect of curing degree on mechanical and thermal properties of 2.5 d quartz fiber reinforced boron phenolic composites. *e-Polymers*, *19*(1), 462–469.

Gebart, B. R. (1992). Permeability of unidirectional reinforcements for rtm. *Journal of composite materials*, *26*(8), 1100–1133.

Gutowski, T., Cai, Z., Bauer, S., Boucher, D., Kingery, J., & Wineman, S. (1987). Consolidation experiments for laminate composites. *Journal of Composite Materials*, *21*(7), 650–669.

Gutowski, T., & Dillon, G. (1992). The elastic deformation of lubricated carbon fiber bundles: comparison of theory and experiments. *Journal of Composite Materials*, *26*(16), 2330–2347.

Heardman, E., Lekakou, C., & Bader, M. (2001). In-plane permeability of sheared fabrics. *Composites Part A: Applied Science and Manufacturing*, *32*(7), 933–940.

HexFlow. (2016). *HexFlow® RTM 6 product data.* Retrieved from `https://www.imatec.it/wp-content/uploads/2016/05/RTM6_global.pdf`

Karkanas, P. I., & Partridge, I. K. (2000). Cure modeling and monitoring of epoxy/amine resin systems. i. cure kinetics modeling. *Journal of applied polymer science*, *77*(7), 1419–1431.

Krogh, C., Bak, B. L., Lindgaard, E., Olesen, A. M., Hermansen, S. M., Broberg, P. H., ... Jakobsen, J. (2021). A simple matlab draping code for fiber-reinforced composites with application to optimization of manufacturing process parameters. *Structural and Multidisciplinary Optimization*, *64*, 457–471.

Kunze, E., Galkin, S., Böhm, R., Gude, M., & Kärger, L. (2020). The impact of draping effects on the stiffness and failure behavior of unidirectional non-crimp fabric fiber reinforced composites. *Materials (Basel)*, *13*(13), 2959. doi: 10.3390/ma13132959

Loendersloot, R. (2011). 8 - permeability of non-crimp fabric preforms. In S. V. Lomov (Ed.), *Non-crimp fabric composites* (p. 166-215). Woodhead Publishing. Retrieved from `https://www.sciencedirect.com/science/article/pii/B9781845697624500084` doi: https://doi.org/10.1533/9780857092533.2.166

Lomov, S., Verpoest, I., Peeters, T., Roose, D., & Zako, M. (2003). Nesting in textile laminates: geometrical modelling of the laminate. *Composites Science and Technology*,

63(7), 993-1007. Retrieved from https://www.sciencedirect.com/science/article/pii/S0266353802003184 doi: https://doi.org/10.1016/S0266-3538(02)00318-4

Masini, A. (2017, May 16). *Mold made of a composite material and process employing this mold.* Google Patents. Retrieved from https://patents.google.com/patent/US9649784 (US Patent 9,649,784 B2, Italian Patent 1405233B1)

McIlhagger, A., Archer, E., & McIlhagger, R. (2020). Manufacturing processes for composite materials and components for aerospace applications. In *Polymer composites in the aerospace industry* (pp. 59–81). Elsevier.

Nettles, A. T. (1994). *Basic mechanics of laminated composite plates* (Tech. Rep.).

Pabsch, A. (1997, February 20). *Vorrichtung und verfahren zur herstellung von großflächigen bauelementen nach dem rtm-verfahren [device and method for producing large-area components using the rtm process].* Google Patents. Retrieved from https://patents.google.com/patent/DE19536675C1 (German Patent 19536675C1)

Prasad, M. S., Watkins, S., Wang, X., Hill, S. S., & Weymouth, D. (2009). Rating criteria for vehicle in-cabin noise with emphasis on hvac system operation. *International Journal of Vehicle Noise and Vibration*, *5*(1-2), 175–191.

Ruzic, D., & Galamboš, S. (2017). Thermal radiation between the driver and the vehicle cabin interior. *Mobility and vehicle mechanics*, *43*(1), 27–37.

Santoni, C. (2019, October 02). *Vehicle body.* Google Patents. Retrieved from https://patents.google.com/patent/EP3357796B1/en?oq=EP3357796B1 (European Patent 3 357 796 B1)

Sasikumar, A., Trias, D., Costa, J., Blanco, N., Orr, J., & Linde, P. (2019). Impact and compression after impact response in thin laminates of spread-tow woven and non-crimp fabrics. *Composite Structures*, *215*, 432-445. Retrieved from https://www.sciencedirect.com/science/article/pii/S0263822318341783 doi: https://doi.org/10.1016/j.compstruct.2019.02.054

Schenk, M. (2023). Handout 3 - classical laminate theory. In *Composite laminate analysis.*

Skramstad, J. D. (1999). *Evaluation of hand lay-up and resin transfer molding in composite wind turbine blade manufacturing* (Unpublished doctoral dissertation). Montana State University-Bozeman, College of Engineering.

Smith, P., Rudd, C., & Long, A. (1997). The effect of shear deformation on the processing and mechanical properties of aligned reinforcements. *Composites Science and Technology*, *57*(3), 327–344.

Svantek. (n.d.). *Body vibration effects on humans.* Retrieved from https://svantek.com/uk/academy/body-vibration-effects-on-humans/ (Accessed on 04/12/23)

Thomson Jr., M. W. (1970, December 29). *Automobile body construction.* Google Patents. Retrieved from https://patents.google.com/patent/US3550948 (US Patent 3,550,948)

Vallons, K. (2015). 12 - fatigue of non-crimp fabric composites. In V. Carvelli & S. V. Lomov (Eds.), *Fatigue of textile composites* (p. 275-293). Woodhead Publishing. Retrieved from https://www.sciencedirect.com/science/article/pii/B9781782422815000122 doi: https://doi.org/10.1016/B978-1-78242-281-5.00012-2

Verrey, J., Wakeman, M., Michaud, V., & Månson, J.-A. (2006). Manufacturing cost comparison of thermoplastic and thermoset rtm for an automotive floor pan. *Composites Part A: Applied Science and Manufacturing*, *37*(1), 9-22. Retrieved from https://www.sciencedirect.com/science/article/pii/S1359835X05002320 doi: https://doi.org/10.1016/j.compositesa.2005.05.048

Wang, B., Fan, S., Chen, J., Yang, W., Liu, W., & Li, Y. (2023). A review on prediction and control of curing process-induced deformation of continuous fiber-reinforced thermosetting composite structures. *Composites Part A: Applied Science and Manufacturing*, *165*, 107321. Retrieved from https://www.sciencedirect.com/science/article/pii/S1359835X22005024 doi: https://doi.org/10.1016/j.compositesa.2022.107321

Xu, J., Lomov, S. V., Verpoest, I., Daggumati, S., Van Paepegem, W., & Degrieck, J. (2016). A comparative study of twill weave reinforced composites under tension–tension fatigue loading: Experiments and meso-modelling. *Composite Structures*, *135*, 306–315.